Local circuit allowing hypothalamic control of hippocampal area CA2 activity and consequences for CA1

Vincent Robert, Ludivine Therreau, Vivien Chevaleyre, Eude Lepicard, Cécile Viollet, Julie Cognet, Arthur Jy Huang, Roman Boehringer, Denis Polygalov, Thomas Mchugh, et al.

Local circuit allowing hypothalamic control of hippocampal area CA2 activity and consequences for CA1

Vincent Robert[1], Ludivine Therreau[1], Vivien Chevaleyre[1,2], Eude Lepicard[1], Cécile Viollet[1], Julie Cognet[1], Arthur J.Y. Huang[3], Roman Boehringer[3], Denis Polygalov[3], Thomas McHugh[3], and Rebecca A. Piskorowski[1,2*]

[1] Université de Paris, INSERM UMR1266, Institute of Psychiatry and Neuroscience of Paris, Team Synaptic Plasticity and Neural Networks, 102-108 rue de la Santé, 75014, Paris, France

[2] GHU Paris Psychiatrie and Neurosciences, 75014 Paris, France

[3]Laboratory for Circuit and Behavioral Physiology, RIKEN Center for Brain Science, 2-1 Hirosawa, Wakoshi, Saitama, Japan

* Corresponding author email: rebecca.piskorowski@u-paris.fr

Abstract

The hippocampus is critical for memory formation. The hypothalamic supramammillary nucleus (SuM) sends long-range projections to hippocampal area CA2. While the SuM-CA2 connection is critical for social memory, how this input acts on the local circuit is unknown. We found that SuM axon stimulation elicited mixed excitatory and inhibitory responses in area CA2 pyramidal neurons (PNs). Parvalbumin-expressing basket cells were largely responsible for the feedforward inhibitory drive of SuM over area CA2. Inhibition recruited by the SuM input onto CA2 PNs increased the precision of action potential firing both in conditions of low and high cholinergic tone. Furthermore, SuM stimulation in area CA2 modulated CA1 activity, indicating that synchronized CA2 output drives a pulsed inhibition in area CA1. Hence, the network revealed here lays basis for understanding how SuM activity directly acts on the local hippocampal circuit to allow social memory encoding.

Introduction

The hippocampus is critical for memory formation and spatial navigation (Buzsáki and Moser, 2013; Eichenbaum and Cohen, 2014), yet basic questions persist regarding the underlying circuitry and cellular components. While area CA2 has been shown to play a significant role in several hippocampal processes including social memory formation (Hitti and Siegelbaum, 2014; Stevenson and Caldwell, 2014) sharp-wave ripple generation (Oliva et al., 2016a) and spatial encoding (Kay et al., 2016), information about the local circuitry and cellular mechanisms allowing these functions is lacking. There is mounting evidence that generalizations cannot be made from the rich understanding of areas CA1 and CA3, as neurons in area CA2 have been shown to have unique molecular expression profiles (Cembrowski et al., 2016; Lein et al., 2004), morphology (Bartesaghi and Ravasi, 1999; No, 1934) and cellular properties (Robert et al., 2020; Srinivas et al., 2017; Sun et al., 2014). Notably, and in contrast to area CA1, CA2 pyramidal neurons do not undergo high frequency stimulation-induced synaptic plasticity (Dasgupta et al., 2020; Zhao et al., 2007). Rather, the excitability of this region is tightly controlled by a highly plastic network of inhibitory neurons (Leroy et al., 2017; Nasrallah et al., 2015; Piskorowski and Chevaleyre, 2013). When active, CA2 pyramidal neurons (PNs) can strongly drive area CA1 (Chevaleyre and Siegelbaum, 2010; Kohara et al., 2014; Nasrallah et al., 2019), thereby influencing hippocampal output. Furthermore, CA2 neurons also project to area CA3, where they recruit inhibition (Boehringer et al., 2017; Kohara et al., 2014) and act to control hippocampal excitability. Thus, CA2 neurons are poised to have long-reaching effects in the hippocampus, and a better understanding of the regulation of neuronal activity in this region is needed.

The hypothalamic supramammillary (SuM) nucleus sends projections to both area CA2 and the dentate gyrus (DG) (Haglund et al., 1984; Vertes, 1992). These long-range connections have been shown in several species including rodents, primates and humans (Berger et al., 2001; Haglund et al., 1984; Wyss et al., 1979) where they are present in early hippocampal development. The SuM has been found to be active during a wide variety of conditions including novel environment exposure (Ito et al., 2009), reinforcement learning (Ikemoto, 2005; Ikemoto et al., 2004), food anticipation (May et al., 2019), and during REM sleep and arousal (Pedersen et al., 2017; Renouard et al., 2015). This nucleus is also known for participating in hippocampal theta rhythm (Pan and McNaughton, 2002, 1997), possibly by its direct projection to the hippocampus or by modulation of the medial septum (Borhegyi et al., 1998; Vertes and Kocsis, 1997), and regulating spike-timing between hippocampus and the cortex (Ito et al.,

2018). Disruption of SuM neuron activity with pharmacological methods (Aranda et al., 2008; Shahidi et al., 2004) or lesions (Aranda et al., 2006) has been reported to disrupt hippocampal memory. Serotonin depletion of the SuM leads to deficiencies in spatial learning in the Morris water maze, and results in altered hippocampal theta activity (Gutiérrez-Guzmán et al., 2012; Hernández-Pérez et al., 2015). Salient rewarding experiences also activate the SuM, as evidenced by cFos expression in monoaminergic SuM neurons by consumption of rewarding food (Plaisier et al., 2020). Furthermore, the rewarding aspects of social aggression have been shown to involve an excitatory circuit between the hypothalamic ventral premammillary nucleus and the SuM (Stagkourakis et al., 2018). It has recently been shown that there are two separate populations of cells in the SuM that target either CA2 or the DG (Chen et al., 2020). In the DG, the SuM terminals release both glutamate and GABA (Boulland et al., 2009; Chen et al., 2020; Hashimotodani et al., 2018; Pedersen et al., 2017; Soussi et al., 2010). The SuM-DG projection has been recently shown to play a role in modulating DG activity in response to contextual novelty (Chen et al., 2020) and spatial memory retrieval (Li et al., 2020). In contrast, functional studies of the SuM-CA2 projection have found that this connection is entirely glutamatergic (Chen et al., 2020). It was recently discovered that the CA2-projecting SuM neurons are active during social novelty exposure, and their selective stimulation prevents expression of a memory of a familiar conspecific (Chen et al., 2020). These findings strongly suggest that the SuM-CA2 connection conveys a social novelty signal to the hippocampus. Furthermore, recent *in vivo* recordings from the SuM in anaesthetized rats reported that a subset of SuM neurons were active earlier than CA2 and other hippocampal cells during SWR (Vicente et al., 2020), indicating a possible role for the SuM-CA2 projection in shaping area CA2 activity prior to SWR onset.

Even with the anatomical and *in vivo* data, the properties and consequences of SuM activation on area CA2 activity remain unexplored. In this study, we use a combination of approaches to specifically examine the effects of SuM input stimulation on neuronal activity in hippocampal area CA2. Here, we show that the SuM-evoked post-synaptic excitation of CA2 PN is controlled by SuM-driven inhibition. We identified PV-expressing basket cells as the neuronal population most strongly excited by SuM input in area CA2, and thus likely responsible for the feedforward inhibition evoked by SuM in CA2 PNs. We found that recruitment of this inhibition enhances the precision of AP firing by area CA2 PNs in conditions of low and high cholinergic tone. Finally, we observed that the resulting synchronized CA2 PN activity drives inhibition in area

CA1, thereby providing a circuit mechanism through which SuM can modulate hippocampal excitability by controlling area CA2 output.

Results

SuM axons provide excitatory glutamatergic input to pyramidal neurons in area CA2 and CA3a

Its small size and cellular heterogeneity have made the SuM a difficult region to study. It has been shown that the source of vesicular glutamate transporter 2 (VGluT2)-immunopositive boutons in area CA2 originate from the SuM (Halasy et al., 2004). In order to more closely examine the SuM-CA2 long-range connection, we injected a retrograde canine adenovirus type 2 (CAV-2) into area CA2 of the hippocampus to permit the expression of Cre-recombinase (Cre) in hippocampal-projecting SuM neurons, and an adeno-associated virus (AAV) was injected into the SuM to allow the expression of EGFP under the control of Cre (Supplemental Figure 1A). In 5 animals the injection of retrograde CAV-2 was sufficiently targeted to area CA2, as indicated by the presence of EGFP-expressing SuM axonal fibers primarily in this hippocampal area (Supplemental Figure 1B). We stained for calretinin to define the boundaries of the SuM nucleus (Pan and Mcnaughton, 2004). Consistent with recent findings using retrograde AAV vectors (Chen et al., 2020), we observed that CA2-projecting cells express calretinin and are located in the medial SuM (Supplemental figure 1C-D). These cells were located bilaterally, ventral to the fiber bundles that traverse the SuM (Supplemental Figure 1C). Furthermore, we confirmed that these cells also stain for VGluT2 (Supplemental figure 1E).

In order to better understand the cellular targets and consequences of SuM input activity in area CA2, we injected an AAV to express channelrhodopsin(H143R)-YFP (ChR2-EYFP) under the control of Cre into the SuM of a transgenic mouse line with Cre expression controlled by the VGluT2 promoter, the Tg(Slc17ab-icre)10Ki line (Borgius et al., 2010) (Supplemental Figure 1F). In parallel, we used the Csf2rb2-Cre mouse line that selectively expresses Cre in the SuM (Chen et al., 2020) (Figure 1A). We found that with both transgenic mouse lines we could reproducibly restrict expression of ChR2-EYFP in the SuM and avoid infecting nearby hypothalamic regions that also project to the hippocampus (Figure 1A, Supplemental Figure 1F). Furthermore, with both lines of transgenic mice, we observed identical patterns of SuM fiber localization in the hippocampus. EYFP-containing SuM axons were found throughout the granule cell layer of the DG and in area CA2 (Figure 1B) where they clustered around the pyramidal layer (*stratum pyramidale*, SP). The SuM fiber projection area was clearly restricted

to area CA2, as defined by expression of the CA2-specific markers PCP4 (Supplemental Figure 1B) and RGS14 (Figure 1B), and did not spread to neighboring areas CA3 and CA1. In order to maximize the precision of our experiments, we frequently only achieved partial infection of the SuM, as indicated by the sparseness of ChR2-EYFP-containing fibers in comparison to the number of VGluT2-stained boutons in this region (Supplemental Figure 1G-H).

We performed whole-cell current and voltage clamp recordings of PNs across the hippocampal CA regions and activated projecting axons with pulses of 488 nm light in acute hippocampal slices. Following all recordings, we performed post-hoc anatomical reconstructions of recorded cells and axonal fibers, as well as immunohistochemical staining for CA2-area markers. Additionally, injection sites were examined *post hoc* to ensure correct targeting of the SuM.

We observed that photostimulation of SuM axons elicited excitatory post-synaptic responses in 63 % of PNs (n = 166 of 263 cells) located in area CA2. PNs in this region shared similar overall dendritic morphologies and electrophysiological properties (Table 1) but differed along two criteria. First, in *stratum lucidum* where the DG mossy fibers (MF) project, some PNs clearly had thorny excrescences (TE) while others had very smooth apical dendrites (Figure 1C-D). Based on the presence of TEs, we classified cells as CA2 or CA3a PNs (unequivocal distinction was possible for 148 neurons). Second, the distribution of the locations of PN soma along the radial axis of the hippocampus allowed us to cluster them as deep (closer to *stratum oriens*, SO) or superficial (closer to *stratum radiatum*, SR) subpopulations (unequivocal distinction was possible for 157 neurons). We found that the SuM-PN connectivity was not different between CA2 and CA3 PNs (Table 2, χ^2 test for CA2 and CA3 PNs, $p = 0.572$) or between deep and superficial PNs (Table 2, χ^2 test for deep and superficial PNs, $p = 0.946$). Light-evoked excitatory post-synaptic potentials (EPSPs) and excitatory post-synaptic currents (EPSCs) recorded at -70mV were of fairly small amplitude (Figure 1C-D) that were similar regardless of the PN type or somatic location (Table 2, Mann-Whitney U test for CA2 and CA3 PNs, $p = 0.409$; Mann-Whitney U test for deep and superficial PNs, $p = 0.306$). Because no significant differences in post-synaptic responses to SuM input stimulation were observed between CA2 and CA3 PNs as well as between deep and superficial PNs, data from all PNs was pooled for the rest of the study. The small amplitude of SuM input-evoked post-synaptic responses in PNs was not due to suboptimal stimulation of SuM axons as EPSC amplitudes rapidly reached a plateau when increasing light intensity (Supplemental Figure 2A-B). We are confident that this transmission is due to action potential-generated vesicle release because all transmission was blocked following application of the sodium channel blocker tetrodotoxin (TTX)

(Supplemental Figure 2B). The pure glutamatergic nature of the SuM input was confirmed by the complete block of light-evoked synaptic transmission following the application of the AMPA and NMDA receptors antagonists NBQX and D-APV (Supplemental Figure 2C; amplitudes were -16 ± 4.8 pA in control and -1.8 ± 0.3 pA in NBQX & D-APV, n = 6; Wilcoxon signed-rank test, p = 0.03). These data confirm that SuM inputs provide long-range glutamatergic excitation to CA2 and CA3 PNs in area CA2.

PNs in area CA2 receive mixed excitatory and inhibitory responses from the SuM input

Using whole-cell voltage clamp recordings in area CA2 and the dentate gyrus (DG), we have previously shown that the CA2-targeting and DG-targeting SuM neurons have contrasting neurotransmitter modalities (Chen et al., 2020). Our results and other have demonstrated that glutamate and GABA are co-released at SuM-DG synapses (Boulland et al., 2009; Chen et al., 2020; Hashimotodani et al., 2018; Pedersen et al., 2017; Soussi et al., 2010), but that the SuM-CA2 synapses are exclusively glutamatergic (Chen et al., 2020). We have previously shown that SuM input stimulation in area CA2 evokes a very large inhibitory post synaptic current (IPSC) that is entirely due to feed-forward inhibition based on the delayed response latencies of IPSCs as compared to EPSCs, the complete block of IPSCs by NBQX and APV, and the complete abolition of IPSCs but sparing of EPSCs in the presence of TTX and 4-amino pyridine (Chen et al., 2020). Because photostimulation of SuM input elicited excitatory post-synaptic potentials (PSPs) of fairly small amplitude in area CA2 PNs held at -70 mV (Figure 1C4 and D4), we asked if the amplitude of SuM input stimulation-evoked PSPs in PNs could be controlled by feed-forward inhibition. Interestingly, blocking inhibitory transmission with the $GABA_A$ and $GABA_B$ receptor antagonists SR95531 and CGP55845A led to a significant increase of light-evoked PSP amplitude recorded in area CA2 PNs (Figure 2A-C; amplitudes of the first response were 0.18 ± 0.05 mV in control and 0.24 ± 0.05 mV in SR95531 & CGP55845A, n = 14; Wilcoxon signed-rank tests, p = 0.004 for the first PSP, p = 0.013 for the second PSP, p < 0.001 for the third PSP). Thus, this result demonstrates a negative control of SuM-driven excitation by feedforward inhibition.

Given the combination of direct excitation and feed-forward inhibition from SuM inputs onto CA2 pyramidal cells, we asked how this input would summate with other synaptic inputs in the CA2 dendritic arbor. Hippocampal area CA2 receives synaptic input from CA3 in *stratum radiatum* (SR). Stimulation of CA3 inputs evokes a very strong feed-forward inhibition, such that it is exceptionally difficult to evoke action potential firing in CA2 pyramidal neurons when inhibitory transmission is intact (Chevaleyre and Siegelbaum, 2010; Nasrallah et al., 2015;

Piskorowski and Chevaleyre, 2013). Additionally, CA2 PNs receive synaptic input from the entorhinal cortex in *stratum lacunosum molecular* (SLM). These inputs are very distal but relatively less attenuated in CA2 PNs in comparison to distal inputs in CA1 (Chevaleyre and Siegelbaum, 2010; Srinivas et al., 2017). In order to answer how the SuM input interacts with the CA3 and entorhinal inputs in area CA2, we electrically stimulated synaptic inputs in SR and SLM in the presence and absence of simultaneous SuM fiber stimulation (Figure 2D). In summary, we found that when the CA2 PNs were kept at -70 mV, SuM input stimulation paired with SR or SLM input had a net depolarizing effect. We measured the amplitudes of the light-evoked SuM PSP, the electrically evoked PSP of either SR or SLM stimulation and the paired SuM and electrical PSP (Figure 2E). For SR input stimulation, we found no significant difference between the observed paired SR + SuM amplitude and the calculated linear summated amplitude (SR alone + SuM alone) (Figure 2F). This was observed for all 4 pulses of input summations delivered at 10 Hz. However, for the SLM input stimulation, the observed paired amplitude was significantly smaller than the linear summation of the two inputs (SLM alone + SuM alone) for the first stimulus ($n = 10$; T test, $p = 0.014$) (Figure 2F). This observation is expected, as the attenuation of distal dendritic SLM inputs causes the peak of the PSP to be delayed relative to the more somatic SuM input. Thus, the SuM input paired with either SR or SLM input stimulation has minor depolarizing effect on the PSP in CA2 PNs. However, the SuM input might have different effect on the SR and SLM inputs depending on the precise timing of their activation.

We also examine the summation ratio for a train of 4 PSPs at 10 Hz from SR and SLM synaptic inputs stimulation with and without simultaneous SuM input stimulation (Figure 2G-H). We observed a significant reduction of the summation ratio as measured by the ratio of the n-th pulse to the first (Pn/P1) for both SR ($n = 10$; repeated-measures ANOVA, $p = 2.3 \times 10^{-4}$) and SLM ($n = 10$; repeated-measures ANOVA, $p = 8.5 \times 10^{-4}$). This observation that concomitant SuM activity is reducing the level of facilitation of several pulses in a train indicates that the short-term dynamics of the SuM-driven excitation and feed-forward inhibition are playing a role to prevent cellular excitation from other inputs.

Basket cells are strongly recruited by the SuM input

Because the hippocampus hosts a variety of interneurons (INs) that are involved in controlling specific aspects of PN excitability, we wished to establish which kind of IN was targeted by the SuM input to area CA2. We performed whole-cell recordings from INs in this area and assessed post-synaptic excitatory responses to SuM axons stimulation in these cells (Figure 3). In

contrast with previous reports of an exclusive innervation of PNs by SuM (Maglóczky et al., 1994), we observed robust light-evoked excitatory transmission from SuM axons in 35 out of 62 interneurons (INs) with soma located in SP. Following biocytin-streptavidin staining and anatomical reconstructions of recorded INs (allowing unequivocal identification in 48 neurons), we were able to classify INs based on their physiological properties, somatic location and axonal arborization location. We classified 22 cells as basket cells (BCs) because their axonal arborizations were restricted to SP (Figure 3A). BCs fired APs at high frequency either in bursts or continuously upon depolarizing current injection and showed substantial repolarizing sag current when hyperpolarized (Figure 4A, Table 3). Light-evoked EPSCs and PSPs were readily observed in the vast majority of BCs (Figure 3A, 3C and 3D, Table 4) and reached large amplitudes in some instances. An additional 26 INs with soma in SP were classified as non-BCs because their axon did not target SP (Figure 3B). In our recordings, these cells fired in bursts and showed little sag during hyperpolarizing current injection steps (Table 3). We consistently observed no or very minor light-evoked excitatory transmission onto non-BCs (Figure 3B-C, Table 4). Furthermore, we recorded from 17 INs that had soma in *stratum oriens* (SO) and 9 in *stratum radiatum* (SR). Like non-BCs, these INs did not receive strong excitation from SuM fibers (Table 4). This data is consistent with the conclusion that SuM input preferentially forms excitatory synapses onto basket cells in area CA2.

To fully assess the strength of SuM inputs onto the different cell types, we examined the following parameters for each population: the connectivity, success rate, amplitude, potency, kinetics, and latencies of EPSCs as well as the resulting depolarization of the membrane potential. First, SuM inputs preferentially innervated BCs as evidenced by a higher connectivity of EPSCs in BCs than in PNs or other INs (Table 4). Importantly, excitatory responses had short latencies with limited jitter (Table 4) indicating that the connection was monosynaptic in all cell types. When voltage-clamping cells at -70 mV, light-evoked EPSCs could be compared between different cell populations. However, not every photostimulation gave rise to an EPSC leading to an average success rate that tended to be highest in BCs (Table 4). In addition, BCs appeared to receive more excitation from the SuM input than other cells types, as the amplitude of EPSCs was larger in BCs than in PNs (Table 4). EPSCs recorded in BCs also had faster kinetics than in PNs (Table 4). Interestingly, combining the success rate of EPSCs with their respective amplitudes to compute the potency of the SuM synapses revealed that it was significantly larger in BCs than in PNs and non-BCs (Figure 3C; potencies were -12 ± 1.6 pA for PNs, n = 166; -29 ± 7.8 pA for BCs, n = 18; -5.9 ± 1.5 pA for non-BCs, n = 13; Kruskal-

Wallis test with Dunn-Holland-Wolfe *post hoc* test, $p = 0.022$). Consequently, EPSPs recorded at -70 mV were of larger amplitude in BCs than in PNs and non-BCs (Figure 3D; amplitudes were 0.44 ± 0.06 mV for PNs, $n = 20$; 1.71 ± 0.57 mV for BCs, $n = 10$; 0.53 ± 0.07 mV for non-BCs, $n = 4$; Kruskal-Wallis test with Dunn-Holland-Wolfe *post hoc* test, $p < 0.001$). When recording cell-attached or current-clamping BCs at their resting membrane potential (V_M), photostimulation of SuM axons was able to evoke AP firing (Figure 3E) in multiple instances ($n = 7$ of 13). However, this was never observed in PNs ($n = 0$ of 78), non-BCs ($n = 0$ of 16), SR INs ($n = 0$ of 9) or SO INs ($n = 0$ of 8). These results show that SuM projections to area CA2 preferentially provide excitation to BCs that are likely responsible of the feedforward inhibition observed in PNs. This is in accordance with an efficient control of area CA2 PNs excitation by the SuM inhibitory drive as axons from BCs deliver the feedforward inhibition to the peri-somatic region of PNs, effectively shunting incoming PSPs from both the SuM and from dendritic-targeted inputs in SR and SLM.

Parvalbumin-expressing basket cells mediate the feedforward inhibition driven by SuM

In the hippocampus, BCs express either cholecystokinin (CCK) or parvalbumin (PV) (Klausberger and Somogyi, 2008). We found that in response to a 1 second depolarizing pulse, most BCs that received strong SuM excitatory input displayed very fast AP firing with little accommodation in the AP firing frequency (Figure 4A-B, Table 3). This firing behavior is similar to what has been reported for fast spiking PV-expressing BCs in CA1 (Pawelzik et al., 2002). In contrast, CCK-expressing BCs show a lower firing frequency and more accommodation during the train (Pawelzik et al., 2002). This result suggests that BCs connected by the SuM may be expressing PV. To directly confirm this hypothesis, we performed *post hoc* immunostaining of recorded interneurons that received strong excitation from SuM input. Because of the dialysis inherent to the whole-cell recording conditions, we encountered difficulty staining for multiple cells. However, PV-immunoreactivity could unequivocally be detected in either the soma or dendrites of 7 connected BCs (Figure 4C). Therefore, this data demonstrates that at least a fraction of the recorded BCs connected by the SuM is expressing PV.

Hence, to address whether the lack of PV staining in some cells was a consequence of dialysis or resulted from the fact that non-PV+ BCs are also connected, we made use of different strategies to differentiate PV+ and CCK+ INs. First, we wished to genetically confirm that PV+ INs are involved in the SuM-driven feedforward inhibition of area CA2 PNs. We used inhibitory Gi-DREADD to selectively inhibit PV+ INs in area CA2 while monitoring

feedforward IPSCs from area CA2 PNs in response to SuM stimulation. To achieve that, we injected AAVs expressing a Cre-dependent hM4D(Gi) inhibitory Gi-DREADD in area CA2 of PV-Cre mice together with AAVs expressing ChR2 with a pan-neuronal promoter in the SuM (Figure 5A). While we were able to obtain very specific expression of DREADD in PV+ INs, only a fraction of PV+ INs had detectable DREADD expression as quantified by immunohistochemistry (Figure 5B; fraction of PV+ INs expressing DREADDs in CA2 = 75 ± 3.5 %, n = 13). We observed a substantial reduction of SuM-evoked IPSC amplitude recorded in area CA2 PNs upon application of 10 μM of the Gi-DREADD ligand CNO (Figure 5C; amplitudes were 847 ± 122 pA in control and 498 ± 87 pA in CNO hence a 42 ± 6.0 % block, n = 13; paired-T test, $p < 0.001$). Although we never measured a complete block of inhibitory responses, this result unequivocally places PV+ INs as mediators of the SuM feedforward inhibition of area CA2 PNs. The incomplete block of IPSCs observed in these experiments indicates that either additional non-PV+ INs are recruited by SuM input or that our silencing of PV-mediated feedforward inhibition is incomplete. This could be a consequence of partial infection of PV+ INs in area CA2 by AAVs carrying DREADDs and partial silencing of DREADD-expressing PV+ INs by CNO. To address the latter, we performed whole-cell recordings from Gi-DREADD-expressing CA2 PV+ INs labelled with mCherry and monitored the variations in V_M level and action potential firing to SuM input stimulation before and after CNO application (Supplemental Figure 3A). We found that CNO application caused a significant hyperpolarization of Gi-DREADD-expressing CA2 PV+ INs, albeit modest in magnitude (Supplemental Figure 3B-D; V_M were -55.3 ± 2.3 mV in ACSF and -61.8 ± 2.7 mV in CNO hence a -6.5 ± 2.4 mV hyperpolarization, n = 6; Wilcoxon signed-rank test, $p = 0.031$). While this confirmed the relevance of our silencing strategy, it highlighted the possibility that Gi-DREADD-expressing CA2 PV+ INs may not be fully silenced by CNO. Indeed, we observed residual SuM-evoked AP firing in these cells after CNO application (Supplemental Figure 3D-E). These data indicate that synaptically evoked somatic AP firing is not fully blocked by CNO in Gi-DREADD-expressing CA2 PV+ INs. Because it is difficult to distinguish between partial silencing of PV INs by Gi-DREADDs or recruitment of other types of INs in the SuM-driven feedforwards inhibition, we adopted other complementary strategies to answer this question.

We used a pharmacological strategy to selectively manipulate PV+ INs by targeting their GABA release machinery. In the neocortex, P/Q-type voltage-gated calcium channels are necessary for GABA release from PV+ fast-spiking INs onto PNs (Zaitsev et al., 2007). In

contrast, N-type calcium channels are primarily involved in GABA release from CCK+ INs (Hefft and Jonas, 2005). Thus, we recorded SuM input-evoked EPSCs and IPSCs in CA2 PNs before and after application of the P/Q-type voltage-gated calcium channels specific blocker ω-agatoxin TK (200 nM) (Figure 5D). We observed a near-complete block of IPSCs upon ω-agatoxin TK application (Figure 5D1, IPSC amplitudes were 245.5 ± 92.6 pA in control and 35.0 ± 15.4 pA in ω-agatoxin TK hence a 81.8 ± 3.9 % block, n = 5; paired-T test, $p < 0.001$), suggesting a major contribution from PV+ INs to SuM-driven feedforward inhibition consistent with our previous results. However, we observed that excitatory transmission from SuM axons was also partially blocked by ω-agatoxin TK application, as SuM input-evoked EPSCs were significantly reduced although not abolished (Figure 5D2, EPSC amplitudes were -51.8 ± 5.9 pA in SR95531 & CGP55845A and -26.5 ± 5.4 pA after ω-agatoxin TK hence a 49.6 ± 5.6 % block, n = 6; paired-T test, $p < 0.001$). This observation indicates that glutamate release from SuM axons relies on P/Q-type voltage-gated calcium channels to some degree, thereby complicating the interpretation of the reduction of IPSC amplitude in CA2 PNs.

It has previously been demonstrated that PV+ BC transmission can be strongly attenuated by mu opioid receptor activation (MOR) while CCK+ BC transmission is insensitive to MOR activation (Glickfeld et al., 2008). Thus, we recorded from PNs in area CA2 and examined the sensitivity of light-evoked IPSCs to the application of the MOR agonist DAMGO (Figure 5E). We found that there was a near complete block of the light-evoked IPSC amplitude following 1 μM DAMGO application (Figure 5E1; IPSC amplitudes were 343 ± 123 pA in control and 31 ± 12.4 pA in DAMGO hence a 88 ± 5.0 % block, n = 6 PNs; Wilcoxon signed-rank test, $p = 0.031$), while direct excitatory transmission remained unaffected (Figure 5E2; EPSC amplitudes were -6.7 ± 1.1 pA in SR95531 & CGP55845A and -5.6 ± 0.9 pA after DAMGO, n = 17 PNs; Wilcoxon signed-rank test, $p = 0.19$). While this result is in agreement with our DREADD and ω-agatoxin TK results showing a major contribution of PV+ INs to the SuM-driven feedforward inhibition, it should be noted that the dichotomy between PV+ versus CCK+ INs sensitivity to DAMGO has not been directly verified in area CA2.

It has recently been shown that delta opioid receptors (DORs) are specifically expressed in a fraction of PV+ cells in the hippocampus (Erbs et al., 2012). Furthermore, PV+ INs in area CA2 are the substrate of an iLTD of feedforward inhibition from CA3 mediated by delta opioid receptor (DOR) activation (Nasrallah et al., 2019; Piskorowski and Chevaleyre, 2013). Therefore, we sought to further refine our characterization of the SuM feedforward inhibition by assessing its sensitivity to DOR activation (Figure 5F). Application of 0.5 μM of the DOR

agonist DPDPE led to a long-term reduction of light-evoked IPSCs recorded in area CA2 PNs, similar to the iLTD seen by CA3 input stimulation (Figure 5F1; IPSC amplitudes were 168 ± 28 pA in control and 64 ± 22 pA in DPDPE hence a 61 ± 14 % block by DPDPE, n = 7; paired-T test, p = 0.015), while leaving direct EPSCs unaffected (Figure 5F2; EPSC amplitudes were -4.0 ± 1.6 pA in SR95531 & CGP55845A and -3.1 ± 1.1 pA after DPDPE, n = 7; Wilcoxon signed-rank test, p = 0.22). Further confirming the PV+ nature of INs responsible for the SuM feedforward inhibition, this result reveals that both the local CA3 and long-range SuM inputs converge onto an overlapping population of INs to inhibit area CA2 PNs, thus enabling cross-talk between these routes through synaptic plasticity of PV+ INs. However, since DORs are only expressed in a fraction of PV+ INs and therefore only reduces but does not fully block PV+ IN-mediated GABA release (Nasrallah et al., 2019; Piskorowski and Chevaleyre, 2013), it is difficult to know if the remaining SuM-evoked IPSCs are from PV+ INs not expressing DOR or from other INs recruited by the SuM input.

Altogether, these 4 methods strongly suggest that SuM inputs selectively recruit PV+ interneurons to inhibit CA2 PNs. Although individually each method does not conclusively demonstrate that SuM input exclusively targets PV+ INs, the consistent reduction of SuM-driven feedforward inhibition of CA2 PNs observed with every approach allows us to conclude that PV+ cells are predominantly targeted by SuM inputs in area CA2.

The feedforward inhibitory drive from SuM controls pyramidal neuron excitability

Given SuM axonal stimulation triggers an excitatory-inhibitory sequence in post-synaptic PNs, we asked which effect would prevail on PN excitability. In order to assess this, we mimicked an active state in PNs by injecting constant depolarizing current steps sufficient to sustain AP firing during 1 second while photostimulating SuM axons at 10 Hz (Figure 6A-B). We observed that recruitment of SuM inputs significantly delayed the onset of the first AP (Figure 6C; latency to the first AP were 221 ± 19.9 ms in control and 233 ± 19.1 ms with photostimulation, hence a 12.1 ± 4.3 ms increase upon photostimulation, n = 12; paired-T test, p = 0.016). In addition, given SuM neurons display theta-locked firing *in vivo*, we asked if rhythmic inhibition driven by SuM inputs in area CA2 could pace AP firing in PNs by defining windows of excitability. Indeed, photostimulation of SuM axons at 10 Hz led to a significant decrease of variability in the timing of AP firing by PNs (Figure 6D-E; standard deviations of the first AP timing were 36.9 ± 11 ms in control and 24.7 ± 7.4 ms with photostimulation, hence a 12.3 ± 5.3 ms decrease upon photostimulation, n = 12; Wilcoxon signed-rank tests, $p < 0.001$ for the first AP, p = 0.008 for the second AP, p = 0.004 for the third AP). Both the delay of AP onset

and the reduction of AP jitter stemmed from the feedforward inhibition recruited by SuM inputs as application of $GABA_A$ and $GABA_B$ receptor antagonists abolished these effects of SuM stimulation (Figure 6C-E; latency to the first AP were 232 ± 19.8 ms in SR95531 & CGP55845A and 235 ± 18.0 ms with photostimulation, n = 6; Wilcoxon signed-rank test, p = 0.44; standard deviations of the first AP timing were 11.9 ± 2.0 ms in SR95531 & CGP55845A and 7.1 ± 1.5 ms with photostimulation, n = 6; Wilcoxon signed-rank tests, p = 0.22 for the first AP, p = 0.16 for the second AP, p = 0.09 for the third AP). These results reveal that the purely glutamatergic SuM input, by recruiting feedforward inhibition, has an overall inhibitory effect on PN excitability and can influence the timing and jitter of area CA2 PN action potential firing.

One drawback of these results is that the injection of current steps to evoke action potential firing is not entirely representative of CA2 PN activity, as there is no synaptic input leading to AP firing. It has been reported that the AP discharge of SuM neurons *in vivo* is phase-locked to the hippocampal theta rhythm (Bernat Kocsis and Vertes, 1994). Because theta rhythm is a brain state characterized by elevated levels of acetylcholine, we approximately mimicked these conditions in the hippocampal slice preparation by bath application of 10 μM of the cholinergic agonist carbachol (CCh). Under these conditions, CA2 PNs depolarize and spontaneously fire rhythmic bursts of APs, and the properties of these AP bursts are tightly controlled by excitatory and inhibitory synaptic transmission (Robert et al., 2020). Thus, we decided to examine how SuM input stimulation influenced CA2 PN firing under these conditions.

Because SuM neurons fire in bursts at theta frequency *in vivo* (Kirk et al., 1996), and because the elevated cholinergic tone accompanying theta can activate muscarinic receptors that alter the synaptic release properties of many synapses in the brain, we examined how synaptic transmission from the SuM input to area CA2 was affected by the application of 10 μM carbachol (CCh) (Supplemental Figure 4A) (Kirk et al., 1996; B Kocsis and Vertes, 1994). With GABA receptors blocked to first assess the SuM excitatory transmission only, we observed that CCh decreased the amplitude and increased the PPR of SuM-evoked EPSCs in CA2 PNs (Supplemental Figure 4B). This suggests a decrease of glutamate release by SuM axons induced by CCh. We found similar results for SuM-evoked feedforward inhibitory transmission to CA2 PNs as IPSC amplitude was decreased and PPR increased with CCh application (Supplemental Figure 4C). Next, we examined the relative short-term dynamics of SuM-evoked excitatory and inhibitory transmission to CA2 PNs. For this, both EPSCs and IPSCs were recorded from the same individual CA2 PNs upon repeated SuM input stimulation with 5 pulses delivered at 10 Hz before and after CCh application (Supplemental Figure 4D-G). We observed that both SuM-

evoked EPSCs and IPSCs underwent short-term depression, as evidenced by a decrease in amplitude along the pulse train as well as amplitude ratios between subsequent pulses over the first pulse (Pn/P1) (Supplemental Figure 4D-F, Supplemental Table 1). It is worth noting that the Pn/P1 ratio was similar for EPSCs and IPSCs and that the E/I ratio did not significantly change with repeated SuM input stimulation (Supplemental Figure 4F-G, Supplemental Table 1). This indicates that the SuM influence over CA2 PN may remain overall inhibitory during prolonged SuM input activation. Similarly influencing both EPSCs and IPSCs, application of 10 μM CCh affected these short-term dynamics of the SuM-CA2 PN transmission by decreasing the amplitude of the initial response (Supplemental Figure 4D-E, Supplemental Table 1) but limiting the subsequent short-term depression of SuM-evoked PSCs amplitude (Supplemental Figure 4D-F, Supplemental Table 1). Interestingly, the overall effect of repeated SuM input stimulation on post-synaptic responses in area CA2 PNs was even more biased towards inhibition after CCh application as the E/I ratio of PSCs during the pulse train was lower in CCh as compared to control (Supplemental Figure 4G, Supplemental Table 1), possibly because of a lesser depression of IPSCs as compared to EPSCs (Supplemental Figure 4D-F, Supplemental Table 1) which could be due to a CCh-induced depolarization of INs mediating SuM-evoked feedforward inhibition. Altogether, these observations match with our findings of the SuM input having an overall inhibitory influence over area CA2, and suggest that this effect might be more gradual over time but even stronger in conditions of elevated cholinergic tone.

Under these conditions of elevated cholinergic tone, we asked how the spontaneous AP bursting activity of CA2 PNs would be affected by activation of the SuM input by triggering 10 second-long trains of 0.5 ms light pulses delivered at 10 Hz to stimulate SuM axons at the onset of bursts (Figure 7A). Because of the intrinsic cell-to-cell variability of bursting kinetics, we photostimulated SuM inputs only during interleaved bursts in the same cells. To do this, bursts were detected automatically with an online threshold detection system that started the photostimulation pulse train after the first AP of every alternating burst, starting with the second burst (Figure 7A-B). For analysis, the number of APs and bursting kinetics could be compared within the same cell. We observed a significant decrease in the number of APs fired during a burst when SuM inputs were photostimulated as compared to interleaved control bursts (Figure 7C-D; numbers of APs per burst were 15.2 ± 2.3 in control and 6.9 ± 1.3 with photostimulation, n = 7; paired-T test, p = 0.031). In control bursts, the AP firing rate of CA2 PNs initially increases, and then progressively decreases. In the photostimulation bursts, the initial increase

of AP firing frequency was absent, and the subsequent AP firing frequency was reduced (Figure 7E; 2-way ANOVA on firing rate over time in light-on vs light-off conditions; light factor, $p < 0.001$; time factor, $p < 0.001$; light x time factor, $p = 0.052$).

In the presence of CCh, CA2 PNs undergo a depolarization of the membrane potential that is followed by a period of AP firing as the membrane potential remains depolarized for several seconds, and then slowly hyperpolarizes until the next bursting event (Robert et al., 2020). We observed that photostimulation of SuM inputs resulted in a striking reduction in the amount of time the membrane potential remained depolarized, and this is likely why the burst duration was significantly shorter in bursts with SuM photo-stimulation (Figure 7F-G; burst duration was 4.0 ± 1.1 s in control and 1.6 ± 0.5 s with photostimulation, n = 7; paired-T test, $p = 0.037$). The rate and level of V_M repolarization following bursts were not significantly changed by SuM input photostimulation (V_M repolarization rate was -3.3 ± 0.6 mV/s in control and -3.6 ± 0.7 mV/s with photostimulation, n = 7; paired-T test, $p = 0.601$; post-burst V_M was -62.8 ± 1.7 mV in control and -62.0 ± 2.0 mV with photostimulation, n = 7; paired-T test, $p = 0.173$), however the inter-burst time interval was reduced. Indeed, AP bursts with SuM input activation were followed more rapidly by another burst of APs than the ones without SuM input activation (Figure 7B and 7H; time until next burst was 93 ± 14 s in control and 59 ± 17 s with photostimulation, n = 7; paired-T test, $p = 0.001$), which could be due to both short-term depression of inhibitory transmission after repeated activation during the SuM input photostimulation train and reduced activation of hyperpolarizing and shunting conductances during bursts shortened by SuM input photostimulation. Thus, in our preparation, SuM input activation is able to modify the spontaneous bursting activity of CA2 PNs under conditions of high cholinergic tone.

As SuM input controls burst firing of action potentials and likely paces activity in area CA2, we wondered how the subsequent output of CA2 PNs would affect their post-synaptic targets. Because CA2 PNs strongly project to CA1 PNs, this activity is likely to influence CA1 encoding and hippocampal output. Thus, we examined the consequences of SuM-CA2 input stimulation on area CA1 both *in vivo* and in acute slices treated with CCh to induce spontaneous activity (Figure 8).

ChR2-EYFP was expressed in the SuM of Csf2rb2-Cre mice in a Cre-dependent manner and the mice were implanted with a microdrive targeting tetrodes to region CA1 and an optical fiber to the SuM terminals in CA2 (Figure 8A). Mice were placed in a small box (familiar context) and left free to explore as blue (473 nm) laser light pulses (50 ms pulse width) were applied to

488 the SuM terminals at 10 Hz. Across 23 recording sessions in five mice we found that the
489 activation of SuM terminals in CA2 resulted in a significant and reproducible change in the
490 multiunit spiking activity recorded in the pyramidal cell layer of CA1 on 34 of 55 tetrodes. The
491 firing rate change was similar across individual tetrodes (Figure 8B-C), with a decrease in the
492 normalized firing rate starting shortly after laser onset and continuing for about 10 ms, followed
493 immediately by a rebound-like increase to about 20 % greater than baseline firing rate (Figure
494 8B-C).

495 In order to get a better mechanistic understanding of this observation, we set out to decipher
496 how SuM activity in area CA2 influences CA1 in the hippocampal slice preparation. To this
497 end, we used the same photostimulation protocol used *in vivo* that consisted of light stimulation
498 trains of 50 ms-long pulses delivered at 10 Hz for 1 second, repeated every 10 seconds for 2
499 minutes and interleaved with light-off sweeps of the same duration, with the microscope
500 objective centered on area CA2. Whole-cell patch-clamp recordings of CA1 PNs were obtained
501 in acute hippocampal slices superfused with CCh and subjected to this light stimulation protocol
502 (Figure 8D). We asked what synaptic events may be responsible for the decreased firing of CA1
503 units observed 10 – 20 ms after light onset *in vivo* (Figure 8A-C). Whole-cell recordings of
504 CA1 PNs showed an absence of EPSCs time-locked to the photostimulation in all but one case
505 (n = 11/12) (Figure 8E-F). In contrast, we often (n = 7/12) observed light-evoked IPSCs in CA1
506 PNs occurring 10 – 20 ms after light onset (Figure 8G-H). Therefore, the reduction in firing of
507 CA1 units *in vivo* is likely caused by increased inhibitory inputs onto CA1 PNs within 10 – 20
508 ms of SuM fiber stimulation over area CA2. This result highlights a contribution of SuM input
509 to controlling CA2 output that regulate CA1 activity *in vivo* and provides a mechanistic
510 interpretation of this observation at the circuit level.

511

512 **Discussion**

513 In this study, we provide direct evidence for a functional connection between the hypothalamus
514 and the hippocampus. Using stereotaxic injection of viral vectors in combination with
515 transgenic mouse lines to express channelrhodopsin in a projection-specific manner, we have
516 been able to selectively stimulate SuM axons in area CA2 of the hippocampus, allowing for the
517 direct examination of synaptic transmission. This approach yielded novel functional
518 information about the SuM input post-synaptic targets and the overall physiological
519 consequences of its activation. We found that, in contrast to previous anatomical reports, SuM
520 input forms synapses onto both PNs and INs in area CA2. The excitatory drive evoked by light-

stimulation of SuM input was significantly larger for BC INs, which we demonstrate are likely PV+. The resulting feedforward inhibition recruited by SuM input stimulation enhanced the precision of AP timing of CA2 PNs in conditions of low and high cholinergic tone relevant to different brain states. The modified CA2 output evoked poly-synaptic inhibition in area CA1, likely responsible for a decrease in firing rate of CA1 units *in vivo*. Overall, we demonstrate that SuM input controls CA2 output to area CA1 by recruiting feedforward inhibition.

SuM input to area CA2 forms a microcircuit where PV+ basket cells strongly inhibit pyramidal neurons

Glutamatergic innervation of area CA2 by the SuM has been previously described by tracing studies (Kiss et al., 2000; Soussi et al., 2010) and presumed to form synapses exclusively onto PNs (Maglóczky et al., 1994). Our experimental strategy allowed for the direct examination of the post-synaptic targets of SuM glutamatergic axons. Our results confirm that PNs in area CA2 indeed receive excitatory synapses from SuM axons. However, in contrast to what had been proposed in previous studies, we observed that SuM inputs target not only PNs but also INs in area CA2. Importantly, we identified a specific subpopulation of INs as BCs which were the cell type most potently excited by SuM. These BCs could fire action potentials upon SuM input photostimulation leading to a substantial feedforward inhibition of neighboring PNs. We found that at resting membrane potentials, the mixed excitatory/inhibitory SuM input resulted in a net depolarization of the membrane potential in CA2 PNs. However, when the SuM input was paired with either inputs in SR or SLM, we observed a decrease in the summation ratios of trains of synaptic inputs consistent with a perisomatic shunting inhibition driven by SuM in area CA2. Furthermore, we found that with elevated cholinergic tone, recruitment of BCs by SuM controlled PNs excitability and shaped spontaneous burst firing. This finding demonstrates that SuM activity can pace action potential firing in PNs through recruitment of feedforward inhibition.

The population of INs potently excited by SuM transmission display many features that motivate us to classify them as PV+ BCs. They have somas located in the somatic layer, have densely packed perisomatic-targeted axons, are fast spiking and show PV immuno-reactivity. The selective expression of GiDREADD in PV+ cells allows for selective silencing that reduces SuM-driven feedforward inhibition of area CA2 PNs. With these techniques, however, we were unable to sufficiently silent PV+ cells in area CA2, leaving open the possibility that another population of basket cell is targeted by SuM input. The feedforward inhibitory transmission recruited by SuM stimulation is highly sensitive to MOR activation. While this supports our

hypothesis that PV+ cells are targeted by SuM input, MORs are not entirely exclusive to PV+ cells (Stumm et al., 2004). We also show that the SuM-recruited feedforward inhibition is sensitive to DOR activation. Unlike MORs, DORs have been shown to be specific to PV+ cells in area CA2, however, only a sub-population of PV+ INs express this receptor (Nasrallah et al., 2019; Piskorowski and Chevaleyre, 2013) leaving open the possibility that the remaining IPSCs evoked by SuM stimulation are not from PV+ cells. We also show in this work that SuM-evoked inhibitory currents are blocked by the application of ω-agatoxin TK, indicating that these recruited INs express P/Q-type CaV channels, consistent with PV+ BCs (Zaitsev et al., 2007). However, we also saw that ω-agatoxin TK also blocked gluatamatergic transmission from SuM inputs, preventing a simple interpretation of these results. Thus, while there is ample evidence that SuM inputs target PV+ BCs in area CA2, we cannot exclude the possibility that other populations of BCs, such as CCK+ INs are also targeted by these inputs. PV+ BCs in the hippocampus have been shown to be modulated by CCK (Lee et al., 2011) which would have very interesting implications for the effect of SuM activity in area CA2. Furthermore, it was recently shown that PV+ BCs actively inhibit CCK+ BCs, enabling a complementary perisomatic inhibitory system that allows for brain-state dependent activity during behavior (Dudok et al., 2021)

Recent studies have indicated that the SuM input to CA2 plays a key role in social novelty discrimination (Chen et al., 2020). Our findings are very consistent with the finding that DOR-mediated inhibitory synaptic plasticity of PV+ INs in area CA2 is required for social recognition memory (Domínguez et al., 2019). Furthermore, exposure to a novel conspecific induces a DOR-mediated plasticity in this same inhibitory network in area CA2 (Leroy et al., 2017). Thus, our finding that SuM input acts via PV+ interneurons fits with previous studies and provides a link between social novelty detection and local CA2 hippocampal inhibitory plasticity.

Overall, the local circuitry and consequences of SuM input to area CA2 contrasts with the SuM-DG path (Hashimotodani et al., 2018; Li et al., 2020; Mizumori et al., 1989; Nakanishi et al., 2001). Previously, we have shown that unlike the SuM-DG synapse, the SuM-CA2 synapse is entirely glutamatergic (Chen et al., 2020). In this study we use both a VGluT2-Cre and SuM-Cre mouse lines to demonstrate how the combination of direct excitation and feedforward inhibition regulates CA2 PN AP firing. Our data shows that SuM activity results in synchronized feedforward inhibition from CA2 to CA1 which decreases CA1 PN firing. While our results are very intriguing given the importance of area CA2 in propagation of hippocampal network activity (Oliva et al., 2016a), further questions remain. CA2 PNs also receive

587 excitatory input from DG cells via the mossy fibers (Kohara et al., 2014; Llorens-Martín et al.,
588 2015). It has been postulated that by increasing DG excitability, the SuM may also be indirectly
589 acting on CA2 (Silkis and Markevich, 2020). These circuits merit further exploration.

590

591 Consequences of SuM input on area CA2 output

592 Recent work has demonstrated a strong excitatory drive from area CA2 to CA1 (Chevaleyre
593 and Siegelbaum, 2010; Kohara et al., 2014; Nasrallah et al., 2019). Consequently, modification
594 of CA2 output through synaptic plasticity (Nasrallah et al., 2019) or neuromodulation (Tirko et
595 al., 2018) affects CA1 activity. This observation is critical when considering social memory
596 formation, which is known to depend on CA2 output (Hitti and Siegelbaum, 2014; Stevenson
597 and Caldwell, 2014) and is likely encoded in downstream ventral CA1 (Okuyama et al., 2016).
598 CA2-targeting cells in the SuM have recently been shown to be highly active during novel
599 social exploration (Chen et al., 2020). From our results, we hypothesize that this novel social
600 signal from the SuM, acts via the PV+ inhibitory network in area CA2 to control the timing of
601 CA2 output onto area CA1.

602 By recruiting feedforward inhibition, SuM activity paces and temporally constrains AP firing
603 from CA2 PNs undergoing depolarization. More critically, in conditions of elevated cholinergic
604 tone relevant to SuM activity *in vivo*, CA2 PNs depolarize and fire bursts of APs that can be
605 shaped by SuM input both by controlling AP firing as well as membrane depolarization. While
606 this result was obtained by triggering SuM input stimulation to the onset of burst firing by CA2
607 PNs, *in vivo* and acute slice experiments revealed a consistent influence of CA1 PN AP firing
608 by SuM input to area CA2 regardless of the timing of SuM input stimulation relative to CA2
609 PN AP burst firing. These results demonstrate a powerful control of SuM input over CA2 output
610 when PNs are spontaneously firing bursts of APs, a firing mode that is most efficient at
611 influencing CA1 activity (Tirko et al., 2018). Optogenetic experiments have recently shown
612 that CA2 PNs can drive a strong feedforward inhibition in area CA1 (Kohara et al., 2014;
613 Nasrallah et al., 2019). Although SuM input likely does not directly drive feedforward
614 inhibition in area CA1 (Chen et al., 2020), the recruitment of feedforward inhibition in area
615 CA2 by SuM input activation could curtail the time window of spontaneous firing in CA2 PNs
616 and effectively lead to a synchronized drive of feedforward inhibition by area CA2 over area
617 CA1. We postulate that the concerted IPSC that we detect in area CA1 with SuM fiber
618 photostimulation in area CA2 corresponds to the large decrease in firing that is observed in
619 CA1 multi-unit recordings *in vivo*. Thus, these data provide evidence for a long-range control

of CA2 bursting activity and the consequences in downstream area CA1 in conditions of high cholinergic tone that accompanies theta oscillations *in vivo* during which SuM is active.

Relevance of the SuM input to area CA2 for hippocampal oscillations

The activity of hippocampal neurons is orchestrated by brain rhythms, notably theta and gamma oscillations that are prominent during exploration and linked to the learning and memory functions of the hippocampus (Buzsáki, 2002; Buzsáki and Wang, 2012; Colgin, 2016). The SuM is active during these brain states and contributes to theta oscillations in the hippocampus (Kirk et al., 1996; Kirk and McNaughton, 1993; B Kocsis and Vertes, 1994; McNaughton et al., 1995; Pan and McNaughton, 2002, 1997; Thinschmidt et al., 1995). Here, we show that the SuM controls area CA2 output to CA1 by recruiting PV+ BCs, which are important for both theta and gamma oscillations (Fuchs et al., 2007; Gulyás et al., 2010; Korotkova et al., 2010; Mann and Mody, 2010). Through its perisomatic mono-synaptic excitation and PV+ BC-mediated di-synaptic inhibition of CA2 PNs, the SuM likely contributes to enforcing theta-locked windows of excitability shaping CA2 PNs output. Area CA2 can influence CA1 activity not only by direct projections but also through its interactions with both CA3 (Boehringer et al., 2017) and EC (Chevaleyre and Siegelbaum, 2010; Rowland et al., 2013) which are major contributors to CA1 theta and gamma oscillations (Buzsáki, 2002; Colgin, 2016). CA2 axons target both CA1 *stratum oriens* and *radiatum* (Nasrallah et al., 2019) , thus the CA2 projections to CA1 likely contributes to the theta and slow gamma oscillations observed in these strata in CA1 (Belluscio et al., 2012; Colgin et al., 2009; Schomburg et al., 2014). Indeed, CA2 PNs show theta- and gamma-modulation of their activity (Fernandez-Lamo et al., 2019; Oliva et al., 2016b), and chemogenetic manipulations of their excitability bidirectionally influences hippocampal low gamma power (Alexander et al., 2018). Further, chronic block of CA2 output transmission leads to hippocampal hyperexcitability and disrupts CA1 theta phase preference and spatial coding (Boehringer et al., 2017). Therefore, by providing a theta-locked input shaping CA2 PN activity, the SuM is poised to contribute to oscillatory activity in downstream brain regions receiving CA2 input. Indeed, chemogenetic activation or silencing of SuM glutamatergic neurons respectively increases or decreases theta and gamma power in the EEG (Pedersen et al., 2017). Further, the SuM is involved in coordinating activity between the prefrontal cortex, the thalamus and area CA1 as evidenced by a loss of theta coherence amongst these regions upon SuM optogenetic silencing during a spatial task requiring action planning

(Ito et al., 2018). Altogether, these studies point to the SuM as a crucial component in the regulation of hippocampal oscillations and our findings shed light on an aspect of this circuit.

Gating of area CA2 activity by PV+ INs and significance for pathologies

The density of PV+ INs in area CA2 is strikingly higher than in neighboring areas CA3 and CA1 (Botcher et al., 2014; Piskorowski and Chevaleyre, 2013). This population of INs has been shown to play a powerful role in controlling the activation of CA2 PNs by CA3 inputs (Nasrallah et al., 2015). We show in this study that long-range inputs from the SuM can strongly recruit PV+ BCs, which in turn inhibit PNs in this area. Hence, both intra-hippocampal inputs from CA3 and long-range inputs from the SuM converge onto PV+ INs to control CA2 PN excitability and output.

Postmortem studies have reported losses of PV+ INs in area CA2 in pathological contexts including bipolar disorder (Benes et al., 1998), Alzheimer's disease (Brady and Mufson, 1997), and schizophrenia (Benes et al., 1998; Knable et al., 2004). Consistent with these reports, in a mouse model of the 22q11.2 deletion syndrome, a major risk factor for schizophrenia in humans, we found a loss of PV staining and deficit of inhibitory transmission in area CA2 that were accompanied by impairments in social memory (Piskorowski et al., 2016). We postulate that the PV+ INs altered during pathological conditions may be the same population of PV+ BCs recruited by long-range SuM inputs. Indeed, the DOR-mediated plasticity onto PV+ INs is altered in the 22q11.2 deletion syndrome mouse model, and we show here that a fraction of the PV+ INs targeted by the SuM also express DOR. Thus, the loss of function of PV+ INs in area CA2 could disrupt proper long-range connection between the hippocampus and the hypothalamus and possibly contribute to some of the cognitive impairments observed in schizophrenic patients and animal models. Further, pharmacological mouse models of schizophrenia have reported increased c-fos immunoreactivity in the SuM as well as memory impairments (Castañé et al., 2015). Although several alterations in these models of schizophrenia could lead to deficits of hippocampal-dependent behavior, abnormalities of the SuM projection onto area CA2 appear as a potential mechanism that warrants further investigation.

Materials & Methods

Key Resources Table				
Reagent type (species) or resource	**Designation**	**Source or reference**	**Identifiers**	**Additional information**
genetic reagent (Mus. musculus)	Tg(Slc17ab-icre)10Ki	(Borgius et al., 2010)	Tg(Slc17ab-icre)10Ki ; VGluT2-cre	
genetic reagent (Mus. musculus)	csf2rb2-Cre	(Chen et al., 2020)	csf2rb2-Cre ; SuM-cre	
genetic reagent (Mus. musculus)	Pvalbtm1(cre)Arbr/J (PV-Cre)	Jackson	Stock No. 017320	
genetic reagent (adeno-associated virus)	AAV9.EF1a.DIO.hChR2(H134R).EYFP	Addgene	Addgene20298	
genetic reagent (adeno-associated virus)	AAV9.hSynapsin.EGFP.WPRE.bGH	Addgene	Addgene 51502	
genetic reagent (adeno-associated virus)	AAV.Synapsin.DIO.hM4D(Gi).mCherry	McHugh Laboratory, Riken		
genetic reagent (adeno-associated virus)	AAV2/9.hSyn.hChR2(H134R).EYFP.WPRE.hGH	Addgene	Addgene 26973	
genetic reagent (Canine adeno virus)	CAV2-cre	Platforme de Vectorologie de Montpellier	CAV Cre	

antibody	anti-RGS14 (mouse monoclonal)	NeuroMab	73-422	1:300
antibody	anti-GFP (chicken polyclonal)	Abcam	ab13970	1:10,000
antibody	anti-VGluT2 (guinea pig polyclonal)	Millipore	AB22	1:10000
antibody	anti-parvalbumin (rabbit polyclonal)	Swant	PV27	1:2000
antibody	anti- PCP4 (rabbit polyclonal)	Sigma	HPA005792	1:600
antibody	anti-Calretinin (mouse monoclonal)	Millipore	MAB1568	1:500
antibody	anti-mCherry (rat monoclonal	Life technologies	M11217	1:5000
other	far-red neurotrace	Life technologies	N21483	1:300
peptide, recombinant protein	Alexa-546-conjugated streptavidin	Life Technologies	S11225	1:500
peptide, recombinant protein	Biocytin	HelloBio	HB5035	4mg / mL

chemical compound, drug	NBQX	HelloBio	HB0443	10 μM
chemical compound, drug	D-APV	HelloBio	HB0225	50 μM
chemical compound, drug	SR95531	Tocris	1262	1 μM
chemical compound, drug	CGP55845A	Tocris	1248	2 μM
chemical compound, drug	DPDPE	Alfa Aesar	J66293	0.5μM
chemical compound, drug	DAMGO	Tocris	1171	1 μM
chemical compound, drug	clozapine N-oxide (CNO)	HelloBio	HB1807	10 μM
chemical compound, drug	Tetrodotoxin (TTX)	Tocris	1078	0.2 μM
chemical compound, drug	Carbamoylcholine chloride (CCh)	Tocris	2810	10 μM
chemical compound, drug	ω-agatoxin TK	Alomone labs	STA-530	200 nM
software, algorithm	Matlab	Mathworks	www.mathworks.com	
software, algorithm	Igor Pro	Wavemetrics	www.wavemetrics.com	
software, algorithm	OriginPro	OriginLab Corporation	www.originlab.com	

software, algorithm	pClamp	Molecular Devices	www.moleculardevices.com	
software, algorithm	Axograph	Axograph	www.axograph.com	

All procedures involving animals were performed in accordance with institutional regulations (French Ministry of Research and Education protocol #12406-2016040417305913). Animal sample sizes were estimated using power tests with standard deviations and ANOVA values from pilot experiments. A 15 % failure rate was assumed to account for stereotaxic injection errors and slice preparation complications. Every effort was made to reduce animal suffering.

Use of the Tg(Slc17ab-icre)10Ki mouse line: we used the Tg(Slc17ab-icre)10Ki mouse line that was previously generated (Borgius et al., 2010) and expresses the Cre recombinase under control of the slc17a6 gene coding the vesicular glutamate transporter isoform 2 (VGluT2).

Use of the csf2rb2-Cre mouse line: We used the csf2rb2-Cre mouse line that was recently generated (Chen et al., 2020) and expresses the Cre recombinase under control of the csf2rb2 gene that shows selective expression in the SuM.

Use of the Pvalbtm1(cre)Arbr/J mouse line: we used the Pvalbtm1(cre)Arbr/J mouse line that was previously generated (Hippenmeyer et al., 2005) and expresses the Cre recombinase under control of the Pvalbm gene coding parvalbumin (PV).

Stereotaxic viral injection: Animals were anaesthetized with ketamine (100 mg/kg) and xylazine (7 mg/kg). The adeno-associated viruses AAV9.EF1a.DIO.hChR2(H134R).EYFP and AAV9.hSynapsin.EGFP.WPRE.bGH were used at $3x10^8$ vg, the AAV.Synapsin.DIO.hM4D(Gi).mCherry was used at $3.6x10^9$ vg and the AAV2/9.hSyn.hChR2(H134R).EYFP.WPRE.hGH was used at $3.7x10^{13}$ vg. The retrograde tracer CAV2-cre virus was used at $2.5x10^{12}$ vg. 500 nL of virus was unilaterally injected into the brain of 4 week-old male wild type C57BL/6, Tg(Slc17ab-icre)10Ki (VGluT2-Cre), csf2rb2-cre (SuM-Cre) or Pvalbtm1(cre)Arbr/J (PV-Cre) mice at 100 nL/min and the injection cannula was left at the injection site for 10 min following infusion. In the case of AAV.Synapsin.DIO.hM4D(Gi)-mCherry injection in PV-Cre mice, bilateral injections were performed in dorsal CA2. The loci of the injection sites were as follows: anterior–posterior relative to bregma: -2.8 mm for SuM, -1.6 mm for CA2; medial-lateral relative to midline: 0

mm for SuM, 1.9 mm for CA2; dorsal-ventral relative to surface of the brain: 4.75 mm for SuM, 1.4 mm for CA2.

Electrophysiological recordings: Transverse hippocampal slices were prepared at least 3 weeks after viral injection and whole-cell patch-clamp recordings were performed from PNs and INs across the hippocampal CA regions. In the case of PV-Cre mice injected with AAV.Synapsin.DIO.hM4D(Gi)-mCherry, slices were prepared 6 weeks after viral injection. Animals were deeply anaesthetized with ketamine (100 mg/kg) and xylazine (7 mg/kg), and perfused transcardially with a N-methyl-D-glucamin-based (NMDG) cutting solution containing the following (in mM): NMDG 93, KCl 2.5, NaH_2PO_4 1.25, $NaHCO_3$ 30, HEPES 20, glucose 25, thiourea 2, Na-ascorbate 5, Na-pyruvate 3, $CaCl_2$ 0.5, $MgCl_2$ 10. Brains were then rapidly removed, hippocampi were dissected out and placed upright into an agar mold and cut into 400 μm thick transverse slices (Leica VT1200S) in the same cutting solution at 4 °C. Slices were transferred to an immersed-type chamber and maintained in artificial cerebro-spinal fluid (ACSF) containing the following (in mM) : NaCl 125, KCl 2.5, NaH_2PO_4 1.25, $NaHCO_3$ 26, glucose 10, Na-pyruvate 2, $CaCl_2$ 2, $MgCl_2$ 1. Slices were incubated at 32°C for approximately 20 min then maintained at room temperature for at least 45 min prior to patch-clamp recordings performed with either potassium- or cesium-based intracellular solutions containing the following (in mM): K- or Cs-methyl sulfonate 135, KCl 5, EGTA-KOH 0.1, HEPES 10, NaCl 2, MgATP 5, Na_2GTP 0.4, Na_2-phosphocreatine 10 and biocytin (4 mg/mL).

ChR2 was excited by 488 nm light delivered by a LED attached to the epifluorescence port of the microscope. Light stimulations trains consisted of 2-10 pulses, 0.5 ms long, delivered at 10 Hz, repeated every 20 s for at least 20 sweeps. Stimulating pipettes filled with ACSF were placed in *stratum radiatum* (SR) of CA1 to antidromically excite CA3-CA2 synapses and in *stratum lacunosum moleculare* (SLM) to stimulate distal dendritic inputs in area CA2. Synaptic currents were evoked with a constant voltage stimulating unit (Digitimer Ltd.) set at 0.1 msec at a voltage range of 5 to 10 V. For the patch-clamp recordings in area CA1 with stimulation of SuM axons in area CA2, 50 ms long light stimulation pulses were delivered every 10 seconds. We used a light intensity of 25 mW/mm^2 which was experimentally determined as the lowest irradiance allowing TTX-sensitive maximal responses in all cell types and conditions. Data were obtained using a Multiclamp 700B amplifier, sampled at 10 kHz and digitized using a Digidata. The pClamp10 software was used for data acquisition. Series resistance were < 20 MOhm and were not compensated in voltage-clamp, bridge balance was applied in current-clamp. An experimentally determined liquid junction potential of approximately 9 mV was not

corrected for. Pharmacological agents were added to ACSF at the following concentrations (in μM): 10 NBQX and 50 D-APV to block AMPA and NMDA receptors, 1 SR95531 and 2 CGP55845A to block $GABA_A$ and $GABA_B$ receptors, 1 DAMGO to activate μ-opioid receptors (MOR), 0.5 DPDPE to activate δ-opioid receptors (DOR), 10 clozapine N-oxide (CNO) to activate hM4D(Gi) DREADDs, 10 CCh to activate cholinergic receptors, 0.2 tetrodotoxin (TTX) to prevent sodic action potential generation, 200 nM ω-agatoxin TK to block P/Q-type voltage-gated calcium channels.

Surgery for *in vivo* recordings: All surgeries were performed in a stereotaxic frame (Narishige). Csf2rb2-cre male mice from 3 to 6 months of age were anaesthetized using 500 mg/kg Avertin. pAAV.DIO.hChR2(H134R).EYFP was injected into the SuM (−2.7 mm AP, +0.4 mm ML, −5.0 mm DV) using a 10 µL Hamilton microsyringe (701LT, Hamilton) with a beveled 33 gauge needle (NF33BL, World Precision Instruments (WPI)). A microsyringe pump (UMP3, WPI) with controller (Micro4, WPI) were used to set the speed of the injection (100 nl/min). The needle was slowly lowered to the target site and remained in place for 5 min prior to start of the injection and the needle was removed 10 min after infusion was complete. Following virus injection, a custom-built screw-driven microdrive containing six independently adjustable nichrome tetrodes (14 µm diameter), gold-plated to an impedance of 200 to 250 kΩ was implanted, with a subset of tetrodes targeting CA1, and an optic fiber (200 µm core diameter, NA=0.22) targeting CA2 (−1.9 mm AP, +/− 2.2 mm ML, −1.6 mm DV). Following recovery, the tetrodes were slowly lowered over several days to CA1 pyramidal cell layer, identified by characteristic local field potential patterns (theta and sharp-wave ripples) and high amplitude multiunit activity. During the adjustment period the animal was habituated every day to a small box in which recording and stimulation were performed.

In vivo recording protocol: Recording was commenced following tetrodes reaching CA1. To examine the impact of SuM terminal stimulation in CA2 the mice were returned to the small familiar box and trains of 10 light pulses (473 nm, 10 mW/mm^2 and pulse width 50 ms) were delivered to the CA2 at 10 Hz. The pulse train was repeated every 10 seconds for at least 20 times as the animals freely explored the box. Multiunit activity was recorded using a DigitalLynx 4SX recording system running Cheetah v.5.6.0 acquisition software (Neuralynx). Broadband signals from each tetrode were filtered between 600 and 6,000 Hz and recorded continuously at 32 kHz. Recording sites were later verified histologically with electrolytic lesions as described above and the position of the optic fiber was also verified from the track.

In Vivo data analysis:

Spike and event timestamps corresponding to onset of each laser pulse were imported into Matlab (MathWorks) and spikes which occurred 50 ms before and 100 ms after each laser pulse were extracted. Raster plots were generated using a 1 ms bin size. Similar results were obtained using 5 ms and 10 ms bin size (data not shown). Firing rate histograms were calculated by dividing total number of spikes in each time bin by that bin's duration. Each firing rate histogram was normalized by converting it into z-score values. Mean standard deviation values for the z-score calculation were taken from pre-laser pulse time period. To average the response across all mice, for each tetrode the firing rate in each bin was normalized to the average rate in the pre-laser period.

Immunochemistry and cell identification:

Midbrains containing the injection site were examined post-hoc to ensure that infection was restricted to the SuM.

Post-hoc reconstruction of neuronal morphology and SuM axonal projections were performed on slices and midbrain tissue following overnight incubation in 4 % paraformaldehyde in phosphate buffered saline (PBS). Midbrain sections were re-sliced sagittally to 100 μm thick sections. Slices were permeabilized with 0.2 % triton in PBS and blocked overnight with 3 % goat serum in PBS with 0.2 % triton. Primary antibody (Life technologies) incubation was carried out in 3 % goat serum in PBS overnight at 4°C. Channelrhodopsin-2 was detected by chicken primary antibody to GFP (Life technologies) (1:10,000 dilution) and an alexa488-conjugated goat-anti chick secondary. Other primary antibodies used were mouse anti-RGS14 (Neuromab) (1:300 dilution), rabbit anti- PCP4 (Sigma) (1:600 dilution), guinea pig anti-VGluT2 antibody (Milipore) (1:10,000 dilution), rabbit anti-parvalbumin antibody (Swant) (1:2000 dilution). Alexa-546-conjugated streptavidin (Life technologies), secondary antibodies and far-red neurotrace (Life technologies) incubations were carried out in block solution for 4 hours at room temperature. Images were collected with a Zeiss 710 laser-scanning confocal microscope.

Reconstructed neurons were classified as either PNs or INs based on the extension and localization of their dendrites and axons. PNs were classified as deep (closest to *stratum oriens*) or superficial (closest to *stratum radiatum*) based on the radial position of their soma in the pyramidal layer. CA1, CA2 and CA3 PNs were identified based on their somatic localization, dendritic arborization and presence of thorny excrescences (TE). Among INs with somas located in the pyramidal layer (*stratum pyramidale*, SP), discrimination between BCs and non-BCs was achieved based on the restriction of their axons to SP or not, respectively. When

available, firing patterns upon injection of depolarizing current step injection, action potential (AP) half-width, amount of repolarizing sag current upon hyperpolarization from -70 mV to -100 mV by current step injection, membrane resistance (R_M) and capacitance (C_M) were additionally used for cell identification. CA2 and CA3a PNs as well as superficial and deep PNs displayed similar firing patterns, AP width, sag current, R_M and C_M; the only statistically difference being a larger R_M of CA3a compared to CA2 PNs which is consistent with previous studies (Chevaleyre and Siegelbaum, 2010; Sun et al., 2017). In contrast, INs had faster firing rates, shorter AP width, higher R_M and lower C_M than PNs. BCs further differed from non-BCs by the presence of a larger sag current. All recorded neurons that could not be unequivocally identified as PNs or INs were excluded from analysis. SuM connectivity to each neuronal population was quantified by dividing the number of cells that displayed a post-synaptic response to SuM input stimulation by the total number of cells sampled for each neuronal population across all recording sessions with successful SuM-CA2 transmission.

Data analysis and statistics: Electrophysiological recordings were analyzed using IGORpro (Wavemetrics) and Clampfit (Molecular devices) software. For accurate measurements of the kinetics and latencies of post-synaptic responses, the following detection process was used. For each cell, average traces were used to create a template waveform that was then fitted to individual traces and measurements were performed on the fitted traces. When only amplitudes of responses were needed, traces were baselined and amplitudes were simply measured at the peak of the responses. Results are reported ± SEM. Statistical significance was assessed using χ^2 test, Student's T test, Mann-Whitney U test, Wilcoxon signed-rank test, Kruskal-Wallis test, one-way or two-way ANOVA where appropriate.

Author Contributions

RAP, VR & TM designed experiments. RAP, VR, VC, LT, EL, RB, AJYH performed experiments. JC and CV provided technical support. VR, RAP, VC and DP completed analysis. VR and RAP wrote the manuscript with input from all authors.

Acknowledgments

Equipment for the IPNP mouse husbandry facility was funded by the *Région Ile de France*. This work was supported by the RIKEN Center for Brain Science (TJM), Grant-in-Aid for Scientific Research from MEXT (19H05646; T.J.M), Grant-in-Aid for Scientific Research on

Innovative Areas from MEXT (19H05233; T.J.M), ANR-13-JSV4-0002-01 (RAP), ANR-18-CE37-0020-01 (RAP), the Ville de Paris Programme Emergences (RAP), and the Brain and Behavioral Research Foundation NARSAD Young Investigator Grant (RAP) and the Foundation Recherche Médicale, FRM:FTD20170437387 and a gift from Schizo-Oui (VR).

References

Alexander GM, Brown LY, Farris S, Lustberg D, Pantazis C, Gloss B, Plummer NW, Jensen P, Dudek SM. 2018. CA2 neuronal activity controls hippocampal low gamma and ripple oscillations. *eLife* **7**:27. doi:10.7554/elife.38052

Aranda L, Begega A, Sánchez-López J, Aguirre JA, Arias JL, Santín LJ. 2008. Temporary inactivation of the supramammillary area impairs spatial working memory and spatial reference memory retrieval. *Physiology Behav* **94**:322–330. doi:10.1016/j.physbeh.2008.01.024

Aranda L, Santín LJ, Begega A, Aguirre JA, Arias JL. 2006. Supramammillary and adjacent nuclei lesions impair spatial working memory and induce anxiolitic-like behavior. *Behav Brain Res* **167**:156–164. doi:10.1016/j.bbr.2005.09.002

Bartesaghi R, Ravasi L. 1999. Pyramidal neuron types in field CA2 of the guinea pig. *Brain research bulletin* **50**:263–273.

Belluscio MA, Mizuseki K, Schmidt R, Kempter R, Buzsáki G. 2012. Cross-Frequency Phase–Phase Coupling between Theta and Gamma Oscillations in the Hippocampus. *J Neurosci* **32**:423–435. doi:10.1523/jneurosci.4122-11.2012

Benes FM, Kwok EW, Vincent SL, Todtenkopf MS. 1998. A reduction of nonpyramidal cells in sector CA2 of schizophrenics and manic depressives. *Biol Psychiat* **44**:88–97. doi:10.1016/s0006-3223(98)00138-3

Berger B, Esclapez M, Alvarez C, Meyer G, Catala M. 2001. Human and monkey fetal brain development of the supramammillary-hippocampal projections: A system involved in the regulation of theta activity. *J Comp Neurol* **429**:515–529. doi:10.1002/1096-9861(20010122)429:4<515::aid-cne1>3.0.co;2-2

Boehringer R, Polygalov D, Huang AJY, Middleton SJ, Robert V, Wintzer ME, Piskorowski RA, Chevaleyre V, McHugh TJ. 2017. Chronic Loss of CA2 Transmission Leads to Hippocampal Hyperexcitability. *Neuron* **94**:642-655.e9. doi:10.1016/j.neuron.2017.04.014

Borgius L, Restrepo CE, Leao RN, Saleh N, Kiehn O. 2010. A transgenic mouse line for molecular genetic analysis of excitatory glutamatergic neurons. *Mol Cell Neurosci* **45**:245–257. doi:10.1016/j.mcn.2010.06.016

Borhegyi Z, Maglóczky Z, Acsády L, Freund TF. 1998. The supramammillary nucleus innervates cholinergic and GABAergic neurons in the medial septum-diagonal band of Broca complex. *Neuroscience* **82**:1053–1065. doi:10.1016/s0306-4522(97)00301-1

Botcher NA, Falck JE, Thomson AM, Mercer A. 2014. Distribution of interneurons in the CA2 region of the rat hippocampus. *Frontiers Neuroanatomy* **8**:104. doi:10.3389/fnana.2014.00104

Boulland J-L, Jenstad M, Boekel AJ, Wouterlood FG, Edwards RH, Storm-Mathisen J, Chaudhry FA. 2009. Vesicular glutamate and GABA transporters sort to distinct sets of vesicles in a population of presynaptic terminals. *Cereb Cortex* **19**:241–248. doi:10.1093/cercor/bhn077

Brady DR, Mufson EJ. 1997. Parvalbumin-immunoreactive neurons in the hippocampal formation of Alzheimer's diseased brain. *Neuroscience* **80**:1113–1125. doi:10.1016/s0306-4522(97)00068-7

Buzsáki G. 2002. Theta oscillations in the hippocampus. *Neuron* **33**:325–340.

Buzsáki G, Moser EI. 2013. Memory, navigation and theta rhythm in the hippocampal-entorhinal system. *Nat Neurosci* **16**:130–138. doi:10.1038/nn.3304

Buzsáki G, Wang XJ. 2012. Mechanisms of gamma oscillations. *Annu Rev Neurosci* **35**:203–225. doi:10.1146/annurev-neuro-062111-150444

Castañé A, Santana N, Artigas F. 2015. PCP-based mice models of schizophrenia: differential behavioral, neurochemical and cellular effects of acute and subchronic treatments. *Psychopharmacology* **232**:4085–4097. doi:10.1007/s00213-015-3946-6

Cembrowski MS, Wang L, Sugino K, Shields BC, Spruston N, Marder E. 2016. Hipposeq: a comprehensive RNA-seq database of gene expression in hippocampal principal neurons. *Elife* **5**:e14997. doi:10.7554/elife.14997

Chen S, He L, Huang AJY, Boehringer R, Robert V, Wintzer ME, Polygalov D, Weitemier AZ, Tao Y, Gu M, Middleton SJ, Namiki K, Hama H, Therreau L, Chevaleyre V, Hioki H, Miyawaki A, Piskorowski RA, McHugh TJ. 2020. A hypothalamic novelty signal modulates hippocampal memory. *Nature* **586**:270–274. doi:10.1038/s41586-020-2771-1

Chevaleyre V, Siegelbaum SA. 2010. Strong CA2 pyramidal neuron synapses define a powerful disynaptic cortico-hippocampal loop. *Neuron* **66**:560–572. doi:10.1016/j.neuron.2010.04.013

Colgin LL. 2016. Rhythms of the hippocampal network. *Nat Rev Neurosci* **17**:239–249. doi:10.1038/nrn.2016.21

Colgin LL, Denninger T, Fyhn M, Hafting T, Bonnevie T, Jensen O, Moser M-B, Moser EI. 2009. Frequency of gamma oscillations routes flow of information in the hippocampus. *Nature* **462**:353–357. doi:10.1038/nature08573

913 Dasgupta A, Lim YJ, Kumar K, Baby N, Pang KLK, Benoy A, Behnisch T, Sajikumar S.
914 2020. Group III metabotropic glutamate receptors gate long-term potentiation and synaptic
915 tagging/capture in rat hippocampal area CA2. *eLife* **9**:919–20. doi:10.7554/elife.55344

916 Domínguez S, Rey CC, Therreau L, Fanton A, Massotte D, Verret L, Piskorowski RA,
917 Chevaleyre V. 2019. Maturation of PNN and ErbB4 Signaling in Area CA2 during
918 Adolescence Underlies the Emergence of PV Interneuron Plasticity and Social Memory.
919 *CellReports* **29**:1099-1112.e4. doi:10.1016/j.celrep.2019.09.044

920 Dudok B, Klein PM, Hwaun E, Lee BR, Yao Z, Fong O, Bowler JC, Terada S, Sparks FT,
921 Szabo GG, Farrell JS, Berg J, Daigle TL, Tasic B, Dimidschstein J, Fishell G, Losonczy A,
922 Zeng H, Soltesz I. 2021. Alternating sources of perisomatic inhibition during behavior.
923 *Neuron* **109**:997-1012.e9. doi:10.1016/j.neuron.2021.01.003

924 Eichenbaum H, Cohen NJ. 2014. Can we reconcile the declarative memory and spatial
925 navigation views on hippocampal function? *Neuron* **83**:764–770.
926 doi:10.1016/j.neuron.2014.07.032

927 Erbs E, Faget L, Scherrer G, Kessler P, Hentsch D, Vonesch J-L, Matifas A, Kieffer BL,
928 Massotte D. 2012. Distribution of delta opioid receptor-expressing neurons in the mouse
929 hippocampus. *Neuroscience* **221**:203–213. doi:10.1016/j.neuroscience.2012.06.023

930 Fernandez-Lamo I, Gomez-Dominguez D, Sanchez-Aguilera A, Oliva A, Morales AV,
931 Valero M, Cid E, Berényi A, Prida LM de la. 2019. Proximodistal Organization of the
932 CA2 Hippocampal Area. *Cell Reports* **26**:1734-1746.e6. doi:10.1016/j.celrep.2019.01.060

933 Fuchs EC, Zivkovic AR, Cunningham MO, Middleton S, Lebeau FEN, Bannerman DM,
934 Rozov A, Whittington MA, Traub RD, Rawlins JNP, Monyer H. 2007. Recruitment of
935 parvalbumin-positive interneurons determines hippocampal function and associated
936 behavior. *Neuron* **53**:591–604. doi:10.1016/j.neuron.2007.01.031

937 Glickfeld LL, Atallah BV, Scanziani M. 2008. Complementary modulation of somatic
938 inhibition by opioids and cannabinoids. *J Neurosci* **28**:1824–1832.
939 doi:10.1523/jneurosci.4700-07.2008

940 Gulyás AI, Szabó GG, Ulbert I, Holderith N, Monyer H, Erdélyi F, Szabó G, Freund TF,
941 Hájos N. 2010. Parvalbumin-containing fast-spiking basket cells generate the field
942 potential oscillations induced by cholinergic receptor activation in the hippocampus. *J*
943 *Neurosci* **30**:15134–15145. doi:10.1523/jneurosci.4104-10.2010

944 Gutiérrez-Guzmán BE, Hernández-Pérez JJ, López-Vázquez MÁ, Fregozo CS, Guevara MÁ,
945 Olvera-Cortés ME. 2012. Serotonin depletion of supramammillary/posterior hypothalamus
946 nuclei produces place learning deficiencies and alters the concomitant hippocampal theta
947 activity in rats. *Eur J Pharmacol* **682**:99–109. doi:10.1016/j.ejphar.2012.02.024

948 Haglund L, Swanson LW, Köhler C. 1984. The projection of the supramammillary nucleus to
949 the hippocampal formation: an immunohistochemical and anterograde transport study with
950 the lectin PHA-L in the rat. *J Comp Neurol* **229**:171–185. doi:10.1002/cne.902290204

951 Halasy K, Hajszan T, Kovács EG, Lam T-T, Leranth C. 2004. Distribution and origin of
952 vesicular glutamate transporter 2-immunoreactive fibers in the rat hippocampus.
953 *Hippocampus* **14**:908–918. doi:10.1002/hipo.20006

954 Hashimotodani Y, Karube F, Yanagawa Y, Fujiyama F, Kano M. 2018. Supramammillary
955 Nucleus Afferents to the Dentate Gyrus Co-release Glutamate and GABA and Potentiate
956 Granule Cell Output. *Cell Reports* **25**:2704-2715.e4. doi:10.1016/j.celrep.2018.11.016

957 Hefft S, Jonas P. 2005. Asynchronous GABA release generates long-lasting inhibition at a
958 hippocampal interneuron-principal neuron synapse. *Nat Neurosci* **8**:1319–1328.
959 doi:10.1038/nn1542

960 Hernández-Pérez JJ, Gutiérrez-Guzmán BE, López-Vázquez MÁ, Olvera-Cortés ME. 2015.
961 Supramammillary serotonin reduction alters place learning and concomitant hippocampal,
962 septal, and supramammillar theta activity in a Morris water maze. *Frontiers Pharmacol*
963 **6**:250. doi:10.3389/fphar.2015.00250

964 Hippenmeyer S, Vrieseling E, Sigrist M, Portmann T, Laengle C, Ladle DR, Arber S. 2005. A
965 Developmental Switch in the Response of DRG Neurons to ETS Transcription Factor
966 Signaling. *Plos Biol* **3**:e159. doi:10.1371/journal.pbio.0030159

967 Hitti FL, Siegelbaum SA. 2014. The hippocampal CA2 region is essential for social memory.
968 *Nature* **508**:88–92. doi:10.1038/nature13028

969 Ikemoto S. 2005. The supramammillary nucleus mediates primary reinforcement via
970 GABA(A) receptors. *Neuropsychopharmacol* **30**:1088–1095. doi:10.1038/sj.npp.1300660

971 Ikemoto S, Witkin BM, Zangen A, Wise RA. 2004. Rewarding effects of AMPA
972 administration into the supramammillary or posterior hypothalamic nuclei but not the
973 ventral tegmental area. *J Neurosci* **24**:5758–5765. doi:10.1523/jneurosci.5367-04.2004

974 Ito HT, Moser EI, Moser M-B. 2018. Supramammillary Nucleus Modulates Spike-Time
975 Coordination in the Prefrontal-Thalamo- Hippocampal Circuit during Navigation. *Neuron*
976 **99**:576-587.e5. doi:10.1016/j.neuron.2018.07.021

977 Ito M, Shirao T, Doya K, Sekino Y. 2009. Three-dimensional distribution of Fos-positive
978 neurons in the supramammillary nucleus of the rat exposed to novel environment.
979 *Neurosci Res* **64**:397–402. doi:10.1016/j.neures.2009.04.013

980 Kay K, Sosa M, Chung JE, Karlsson MP, Larkin MC, Frank LM. 2016. A hippocampal
981 network for spatial coding during immobility and sleep. *Nature* **531**:185–190.
982 doi:10.1038/nature17144

983 Kirk IJ, McNaughton N. 1993. Mapping the differential effects of procaine on frequency and
984 amplitude of reticularly elicited hippocampal rhythmical slow activity. *Hippocampus*
985 **3**:517–525. doi:10.1002/hipo.450030411

986 Kirk IJ, Oddie SD, Konopacki J, Bland BH. 1996. Evidence for differential control of
987 posterior hypothalamic, supramammillary, and medial mammillary theta-related cellular

discharge by ascending and descending pathways. *J Neurosci Official J Soc Neurosci* **16**:5547–54.

Kiss J, Csáki Á, Bokor H, Shanabrough M, Leranth C. 2000. The supramammillo-hippocampal and supramammillo-septal glutamatergic/aspartatergic projections in the rat: a combined [3H]d-aspartate autoradiographic and immunohistochemical study. *Neuroscience* **97**:657–669. doi:10.1016/s0306-4522(00)00127-5

Klausberger T, Somogyi P. 2008. Neuronal diversity and temporal dynamics: the unity of hippocampal circuit operations. *Science* **321**:53–57. doi:10.1126/science.1149381

Knable MB, Barci BM, Webster MJ, Meador-Woodruff J, Torrey EF, Consortium SN. 2004. Molecular abnormalities of the hippocampus in severe psychiatric illness: postmortem findings from the Stanley Neuropathology Consortium. *Mol Psychiatr* **9**:609-20–544. doi:10.1038/sj.mp.4001471

Kocsis Bernat, Vertes RP. 1994. Characterization of neurons of the supramammillary nucleus and mammillary body that discharge rhythmically with the hippocampal theta rhythm in the rat. *J Neurosci* **14**:7040–7052. doi:10.1523/jneurosci.14-11-07040.1994

Kocsis B, Vertes RP. 1994. Characterization of neurons of the supramammillary nucleus and mammillary body that discharge rhythmically with the hippocampal theta rhythm in the rat. *J Neurosci Official J Soc Neurosci* **14**:7040–52.

Kohara K, Pignatelli M, Rivest AJ, Jung H-Y, Kitamura T, Suh J, Frank D, Kajikawa K, Mise N, Obata Y, Wickersham IR, Tonegawa S. 2014. Cell type-specific genetic and optogenetic tools reveal hippocampal CA2 circuits. *Nat Neurosci* **17**:269–279. doi:10.1038/nn.3614

Korotkova T, Fuchs EC, Ponomarenko A, Engelhardt J von, Monyer H. 2010. NMDA receptor ablation on parvalbumin-positive interneurons impairs hippocampal synchrony, spatial representations, and working memory. *Neuron* **68**:557–569. doi:10.1016/j.neuron.2010.09.017

Lee SY, Földy C, Szabadics J, Soltesz I. 2011. Cell-type-specific CCK2 receptor signaling underlies the cholecystokinin-mediated selective excitation of hippocampal parvalbumin-positive fast-spiking basket cells. *J Neurosci* **31**:10993–11002. doi:10.1523/jneurosci.1970-11.2011

Lein ES, Zhao X, Gage FH. 2004. Defining a Molecular Atlas of the Hippocampus Using DNA Microarrays and High-Throughput In Situ Hybridization. *Journal of Neuroscience* **24**:3879–3889. doi:10.1523/jneurosci.4710-03.2004

Leroy F, Brann DH, Meira T, Siegelbaum SA. 2017. Input-Timing-Dependent Plasticity in the Hippocampal CA2 Region and Its Potential Role in Social Memory. *Neuron* **95**:1089-1102.e5. doi:10.1016/j.neuron.2017.07.036

Li Y, Bao H, Luo Y, Yoan C, Sullivan HA, Quintanilla L, Wickersham I, Lazarus M, Shin Y-YI, Song J. 2020. Supramammillary nucleus synchronizes with dentate gyrus to regulate

spatial memory retrieval through glutamate release. *eLife* **9**:604–23. doi:10.7554/elife.53129

Llorens-Martín M, Jurado-Arjona J, Avila J, Hernández F. 2015. Novel connection between newborn granule neurons and the hippocampal CA2 field. *Exp Neurol* **263**:285–292. doi:10.1016/j.expneurol.2014.10.021

Maglóczky Z, Acsády L, Freund TF. 1994. Principal cells are the postsynaptic targets of supramammillary afferents in the hippocampus of the rat. *Hippocampus* **4**:322–334. doi:10.1002/hipo.450040316

Mann EO, Mody I. 2010. Control of hippocampal gamma oscillation frequency by tonic inhibition and excitation of interneurons. *Nat Neurosci* **13**:205–212. doi:10.1038/nn.2464

May MVL, Hume C, Sabatier N, Schéle E, Bake T, Bergström U, Menzies J, Dickson SL. 2019. Activation of the rat hypothalamic supramammillary nucleus by food anticipation, food restriction or ghrelin administration. *Journal of neuroendocrinology* **31**:e12676-14. doi:10.1111/jne.12676

McNaughton N, Logan B, Panickar KS, Kirk IJ, Pan W, Brown NT, Heenan A. 1995. Contribution of synapses in the medial supramammillary nucleus to the frequency of hippocampal theta rhythm in freely moving rats. *Hippocampus* **5**:534–545. doi:10.1002/hipo.450050605

Mizumori SJ, McNaughton BL, Barnes CA. 1989. A comparison of supramammillary and medial septal influences on hippocampal field potentials and single-unit activity. *Journal of Neurophysiology* **61**:15–31.

Nakanishi K, Saito H, Abe K. 2001. The supramammillary nucleus contributes to associative EPSP-spike potentiation in the rat dentate gyrus in vivo. *Eur J Neurosci* **13**:793–800. doi:10.1046/j.1460-9568.2001.01446.x

Nasrallah K, Piskorowski RA, Chevaleyre V. 2015. Inhibitory Plasticity Permits the Recruitment of CA2 Pyramidal Neurons by CA3(1,2,3). *Eneuro* **2**:1–12. doi:10.1523/eneuro.0049-15.2015

Nasrallah K, Therreau L, Robert V, Huang AJY, McHugh TJ, Piskorowski RA, Chevaleyre V. 2019. Routing Hippocampal Information Flow through Parvalbumin Interneuron Plasticity in Area CA2. *Cell Reports* **27**:86-98.e3. doi:10.1016/j.celrep.2019.03.014

No RL de. 1934. Studies on the Structure of the Cerebral Cortex. II. Continuation of the Study of the Ammonic System. *Journal f Psychologie and Neurologie* 113–175.

Okuyama T, Kitamura T, Roy DS, Itohara S, Tonegawa S. 2016. Ventral CA1 neurons store social memory. *Science* **353**:1536–1541. doi:10.1126/science.aaf7003

Oliva A, Fernández-Ruiz A, Buzsáki G, Berényi A. 2016a. Role of Hippocampal CA2 Region in Triggering Sharp-Wave Ripples. *Neuron* **91**:1342–1355. doi:10.1016/j.neuron.2016.08.008

1063 Oliva A, Fernández-Ruiz A, Buzsáki G, Berényi A. 2016b. Spatial coding and physiological
1064 properties of hippocampal neurons in the Cornu Ammonis subregions. *Hippocampus*
1065 **26**:1593–1607. doi:10.1002/hipo.22659

1066 Pan W, McNaughton N. 2002. The role of the medial supramammillary nucleus in the control
1067 of hippocampal theta activity and behaviour in rats. *Eur J Neurosci* **16**:1797–1809.
1068 doi:10.1046/j.1460-9568.2002.02267.x

1069 Pan W-X, Mcnaughton N. 2004. The supramammillary area: its organization, functions and
1070 relationship to the hippocampus. *Prog Neurobiol* **74**:127–166.
1071 doi:10.1016/j.pneurobio.2004.09.003

1072 Pan W-X, McNaughton N. 1997. The medial supramammillary nucleus, spatial learning and
1073 the frequency of hippocampal theta activity. *Brain Res* **764**:101–108. doi:10.1016/s0006-
1074 8993(97)00431-9

1075 Pawelzik H, Hughes DI, Thomson AM. 2002. Physiological and morphological diversity of
1076 immunocytochemically defined parvalbumin- and cholecystokinin-positive interneurones
1077 in CA1 of the adult rat hippocampus. *J Comp Neurol* **443**:346–367. doi:10.1002/cne.10118

1078 Pedersen NP, Ferrari L, Venner A, Wang JL, Abbott SBG, Vujovic N, Arrigoni E, Saper CB,
1079 Fuller PM. 2017. Supramammillary glutamate neurons are a key node of the arousal
1080 system. *Nat Commun* **8**:1–16. doi:10.1038/s41467-017-01004-6

1081 Piskorowski RA, Chevaleyre V. 2013. Delta-opioid receptors mediate unique plasticity onto
1082 parvalbumin-expressing interneurons in area CA2 of the hippocampus. *J Neurosci*
1083 **33**:14567–14578. doi:10.1523/jneurosci.0649-13.2013

1084 Piskorowski RA, Nasrallah K, Diamantopoulou A, Mukai J, Hassan SI, Siegelbaum SA,
1085 Gogos JA, Chevaleyre V. 2016. Age-Dependent Specific Changes in Area CA2 of the
1086 Hippocampus and Social Memory Deficit in a Mouse Model of the 22q11.2 Deletion
1087 Syndrome. *Neuron* **89**:163–176. doi:10.1016/j.neuron.2015.11.036

1088 Plaisier F, Hume C, Menzies J. 2020. Neural connectivity between the hypothalamic
1089 supramammillary nucleus and appetite- and motivation-related regions of the rat brain.
1090 *Journal of neuroendocrinology* jne.12829-31. doi:10.1111/jne.12829

1091 Renouard L, Billwiller F, Ogawa K, Clément O, Camargo N, Abdelkarim M, Gay N, Scoté-
1092 Blachon C, Touré R, Libourel P-A, Ravassard P, Salvert D, Peyron C, Claustrat B, Léger
1093 L, Salin P, Malleret G, Fort P, Luppi P-H. 2015. The supramammillary nucleus and the
1094 claustrum activate the cortex during REM sleep. *Sci Adv* **1**:e1400177–e1400177.
1095 doi:10.1126/sciadv.1400177

1096 Robert V, Therreau L, Davatolhagh MF, Bernardo-Garcia FJ, Clements KN, Chevaleyre V,
1097 Piskorowski RA. 2020. The mechanisms shaping CA2 pyramidal neuron action potential
1098 bursting induced by muscarinic acetylcholine receptor activation. *J Gen Physiol* **152**.
1099 doi:10.1085/jgp.201912462

1100 Rowland DC, Weible AP, Wickersham IR, Wu H, Mayford M, Witter MP, Kentros CG.
1101 2013. Transgenically Targeted Rabies Virus Demonstrates a Major Monosynaptic

1102 Projection from Hippocampal Area CA2 to Medial Entorhinal Layer II Neurons. *J*
1103 *Neurosci* **33**:14889–14898. doi:10.1523/jneurosci.1046-13.2013

1104 Schomburg EW, Fernández-Ruiz A, Mizuseki K, Berényi A, Anastassiou CA, Koch C,
1105 Buzsáki G. 2014. Theta Phase Segregation of Input-Specific Gamma Patterns in
1106 Entorhinal-Hippocampal Networks. *Neuron* **84**:470–485.
1107 doi:10.1016/j.neuron.2014.08.051

1108 Shahidi S, Motamedi F, Naghdi N. 2004. Effect of reversible inactivation of the
1109 supramammillary nucleus on spatial learning and memory in rats. *Brain Res* **1026**:267–
1110 274. doi:10.1016/j.brainres.2004.08.030

1111 Silkis IG, Markevich VA. 2020. Possible Mechanisms of the Influence of the Supramillary
1112 Nucleus on the Functioning of the Dentate Gyrus and the CA2 Field of the Hippocamsus
1113 (Role of Disinhibition). *Neurochem J* **14**:375–383. doi:10.1134/s181971242004011x

1114 Soussi R, Zhang N, Tahtakran S, Houser CR, Esclapez M. 2010. Heterogeneity of the
1115 supramammillary-hippocampal pathways: evidence for a unique GABAergic
1116 neurotransmitter phenotype and regional differences. *Eur J Neurosci* **32**:771–785.
1117 doi:10.1111/j.1460-9568.2010.07329.x

1118 Srinivas KV, Buss EW, Sun Q, Santoro B, Takahashi H, Nicholson DA, Siegelbaum SA.
1119 2017. The Dendrites of CA2 and CA1 Pyramidal Neurons Differentially Regulate
1120 Information Flow in the Cortico-Hippocampal Circuit. *J Neurosci* **37**:3276–3293.
1121 doi:10.1523/jneurosci.2219-16.2017

1122 Stagkourakis S, Spigolon G, Williams P, Protzmann J, Fisone G, Broberger C. 2018. A neural
1123 network for intermale aggression to establish social hierarchy. *Nat Neurosci* **21**:834–842.
1124 doi:10.1038/s41593-018-0153-x

1125 Stevenson EL, Caldwell HK. 2014. Lesions to the CA2 region of the hippocampus impair
1126 social memory in mice. *Eur J Neurosci* **40**. doi:10.1111/ejn.12689

1127 Stumm RK, Zhou C, Schulz S, Höllt V. 2004. Neuronal types expressing mu- and delta-
1128 opioid receptor mRNA in the rat hippocampal formation. *J Comp Neurol* **469**:107–118.
1129 doi:10.1002/cne.10997

1130 Sun Q, Sotayo A, Cazzulino AS, Snyder AM, Denny CA, Siegelbaum SA. 2017.
1131 Proximodistal Heterogeneity of Hippocampal CA3 Pyramidal Neuron Intrinsic Properties,
1132 Connectivity, and Reactivation during Memory Recall. *Neuron* **95**:656-672.e3.
1133 doi:10.1016/j.neuron.2017.07.012

1134 Sun Q, Srinivas KV, Sotayo A, Siegelbaum SA. 2014. Dendritic Na(+) spikes enable cortical
1135 input to drive action potential output from hippocampal CA2 pyramidal neurons. *Elife*
1136 **3**:7750. doi:10.7554/elife.04551

1137 Thinschmidt JS, Kinney GG, Kocsis B. 1995. The supramammillary nucleus: Is it necessary
1138 for the mediation of hippocampal theta rhythm? *Neuroscience* **67**:301–312.
1139 doi:10.1016/0306-4522(95)00045-k

Tirko NN, Eyring KW, Carcea I, Mitre M, Chao MV, Froemke RC, Tsien RW. 2018. Oxytocin Transforms Firing Mode of CA2 Hippocampal Neurons. *Neuron* **100**:593-608.e3. doi:10.1016/j.neuron.2018.09.008

Vertes RP. 1992. PHA-L analysis of projections from the supramammillary nucleus in the rat. *J Comp Neurol* **326**:595–622. doi:10.1002/cne.903260408

Vertes RP, Kocsis B. 1997. Brainstem-diencephalo-septohippocampal systems controlling the theta rhythm of the hippocampus. *Neuroscience* **81**:893–926.

Vicente AF, Slézia A, Ghestem A, Bernard C, Quilichini PP. 2020. In Vivo Characterization of Neurophysiological Diversity in the Lateral Supramammillary Nucleus during Hippocampal Sharp-wave Ripples of Adult Rats. *Neuroscience* **435**:95–111. doi:10.1016/j.neuroscience.2020.03.034

Wyss JM, Swanson LW, Cowan WM. 1979. Evidence for an input to the molecular layer and the stratum granulosum of the dentate gyrus from the supramammillary region of the hypothalamus. *Anat Embryol* **156**:165–176. doi:10.1007/bf00300012

Zaitsev AV, Povysheva NV, Lewis DA, Krimer LS. 2007. P/Q-Type, But Not N-Type, Calcium Channels Mediate GABA Release From Fast-Spiking Interneurons to Pyramidal Cells in Rat Prefrontal Cortex. *J Neurophysiol* **97**:3567–3573. doi:10.1152/jn.01293.2006

Zhao M, Choi Y-S, Obrietan K, Dudek SM. 2007. Synaptic plasticity (and the lack thereof) in hippocampal CA2 neurons. *J Neurosci* **27**:12025–12032. doi:10.1523/jneurosci.4094-07.2007

Figure legends

Figure 1. Selective functional mapping of SuM neurons that project to hippocampal area CA2. A. Left, diagram illustrating the injection of AAVs into the SuM. Middle, sagittal image indicating the infected SuM area expressing hCHR2(H134R)-EYFP (green). Right, expanded view of injection site in the Csf2rbr-Cre mouse line. B. Left, hCHR2(H134R)-EYFP -expressing SuM fibers (green) and nissl staining (blue) in the hippocampus. Right, higher magnification image of area CA2 with hCHR2(H134R)-EYFP -expressing SuM fibers (green) and nissl staining (blue) and RGS14 staining (magenta) to label area CA2. C. CA2 pyramidal neurons in the SuM-innervated region receive excitatory transmission. (C1) Example CA2 PN reconstruction (dendrites in black, axons in grey, hippocampal stratum borders shown in dotted line, area demarcated in blue corresponds to the expanded image in C2). (C2) Biocytin labeling of the recorded cell proximal dendrites, scale bar represents 10 μm. (C3) AP firing and

repolarizing sag current in response to steps of +800 and -400 pA current injection. (C4) Light-evoked EPSPs (top traces, individual traces shown in grey, average trace shown in black) and EPSCs (bottom traces, individual traces shown in grey, average trace shown in black). D. CA3a pyramidal neurons in the SuM-innervated region receive excitatory transmission. (D1) Example CA3 PN reconstruction (dendrites in brown, axons in light brown, hippocampal stratum borders shown in dotted line, area demarcated in blue corresponds to the expanded image in D2). (D2) Biocytin labeling of the recorded cell proximal dendrites, note the presence of thorny excrescences, as indicated by the red arrows; scale bar represents 10 μm. (D3) AP firing and repolarizing sag current in response to steps of +800 and -400 pA current injection. (D4) Light-evoked EPSPs (top traces, individual traces shown in grey, average trace shown in black) and EPSCs (bottom traces, individual traces shown in grey, average trace shown in black).

Figure 2. SuM input drives inhibition that controls excitation in CA2 PNs. Whole-cell current clamp recordings of light-evoked post-synaptic potentials (PSPs) from SuM input stimulation onto CA2 PNs reveal contribution of feed-forward inhibition in dampening excitatory input at -70 mV. A. Diagram illustrating whole-cell recording configuration in acute hippocampal slices. During these experiments, direct current was injected as necessary to maintain a membrane potential of -70 mV. B. Sample traces of three 10 Hz SuM light-evoked PSPs in a CA2 PN before and after blocking inhibitory transmission (control shown in black, SR95531 & CGP55845A in grey). C. Summary graph of light-evoked PSP amplitudes recorded in PNs before and after application of 1 μM SR95531& 2 μM CGP55845A (individual cells shown as thin lines, population average shown as thick line, error bars represent SEM, n = 14; Wilcoxon signed-rank tests, $p = 0.004$ for the first PSP, $p = 0.013$ for the second PSP, $p < 0.001$ for the third PSP). D-H. Summation of SuM synaptic potentials with SR and SLM electrical input stimulation. D. Diagram illustrating the recording configuration similar to panel A but with stimulating electrodes positioned in *stratum lacunosum moleculare* (SLM) and *stratum radiatum* (SR). E. Left, example traces of PSPs evoked by SuM fiber light stimulation alone (blue trace). Center, PSPs evoked by electrical stimulation of SR inputs alone (black) or paired with simultaneous SuM stimulation (orange). Right, PSPs evoked by electrical stimulation of SLM inputs alone (black) or paired with SuM stimulation (green). F, Plots of the difference between the mathematical summation of the amplitudes of the SuM PSP amplitude and electrical stimulation (linear summation) and the measured SuM + electrical PSP. Left, SR inputs are not significantly different from zero, indicating that SuM and SR inputs linearly

summate. Right, for the first pulse, the measured SLM + SuM amplitude is significantly smaller (n = 10; T test, p = 0.014) than the expected linear summation. G. Left, example traces of 10 Hz trains of PSPs of either electrical stimulation (black traces) or trains of paired electrical and light stimulation of SuM fibers (SR + SuM in orange or SLM + SuM in green). Right, traces with amplitudes normalized to the first PSP for both the electrical and simultaneous light and electrical PSPs. The amplitudes for all PSPs are measured from the potential immediately before each stimulus. H. Summary plots of the summation ratio of the 2nd, 3rd and 4th PSP for electrical stimulation (black symbols) or paired stimulation of SR + SuM (left, orange) or SLM + SuM (right, green).

Figure 3. SuM input provides strong excitatory glutamatergic transmission to basket cells (BCs) in area CA2. A-B. Left, diagrams illustrating whole-cell recordings in area CA2 and SuM fiber stimulation in acute slice preparation. Middle, example reconstruction of different cell types (soma and dendrites in thick lines, axon in thin lines, hippocampal strata in dotted grey lines). Right, sample traces of light-evoked EPSPs (top, individual traces in grey, average trace in black) and EPSCs (bottom, individual traces in grey, average trace in black). A. Basket cell in area CA2. B. Non-basket cell in area CA2. C. Summary graph of light-evoked EPSC potencies in PNs, BCs and non-BCs in area CA2 (individual cells shown as dots, population average shown as thick line, error bars represent SEM, PNs: n = 166; BC INs: n = 18; non-BCs: n = 13; Kruskal-Wallis test with Dunn-Holland-Wolfe *post hoc* test, p = 0.022). D. Summary graph of light-evoked PSP amplitudes in PNs, BCs and non-BCs (individual cells shown as dots, population average shown as thick line, error bars represent SEM, PNs: n = 20; BCs: n = 10; non-BCs: n = 4; Kruskal-Wallis test with Dunn-Holland-Wolfe *post hoc* test, p < 0.001). E. Left, proportion of post-synaptic CA2 PNs, BCs and non-BCs firing action potentials time-locked to light stimulation of SuM input. Right, sample traces of light-evoked action potentials in a BC recorded in current-clamp at resting membrane potential (top) and in cell-attached (bottom) configurations.

Figure 4. SuM input provides excitation to Parvalbumin-expressing BCs. A. Three biocytin reconstructions of BC INs with dendrites in red and axons in light red. Inset, current clamp steps to -400 pA and +400 pA display high-frequency AP firing and repolarizing sag current. B. Corresponding light-evoked EPSCs and EPSPs for the three reconstructed neurons (individual traces in grey, average trace in black). C. Corresponding PV immunostaining of the

three interneurons: parvalbumin staining, biocytin labeling of the recorded cell, and merge (PV in magenta and biocytin in green).

Figure 5. Parvalbumin-expressing BCs mediate the feedforward inhibition recruited by photostimulation of SuM fibers. A-C. Silencing of PV+ INs by inhibitory DREADDs reduces SuM feedforward inhibition onto area CA2 PNs. A. Diagram illustrating the method to infect SuM neurons and selectively inhibit PV+ INs in area CA2. An AAV allowing the Cre-dependent expression of inhibitory DREADD was injected bilaterally into area CA2 of the dorsal hippocampus and another AAV allowing the expression of ChR2 was injected into the SuM of PV-Cre mice, allowing optogenetic stimulation of SuM inputs and pharmacogenetic inhibition of PV+ INs by application of the DREADD agonist CNO at 10 μM. B. Example immunostaining against PV, DREADD and biocytin labelling in area CA2 from a slice used in these experiments. C. Left, diagram of the recording configuration in hippocampal slices. Center, sample traces (control in red, CNO in grey). Right, summary graph of light-evoked IPSC amplitudes recorded in CA2 PNs before and after application of 10 μM CNO (n = 13, error bars represent SEM). D. Application of the P/Q-Type voltage activated calcium channel blocker ω-agatoxin TK results in nearly complete loss of feed-forward inhibition recruited by light activation of SuM inputs in area CA2. D1, sample traces, (top, control in red, ω-agatoxin TK in grey) and summary graph of light-evoked IPSC amplitudes recorded in CA2 PNs before and after application of 200 nM ω-agatoxin TK (bottom, n = 5, error bars represent SEM). D2, sample traces (top, SR95531 & CGP55845A in black, ω-agatoxin TK in grey) and summary graph of light-evoked EPSC amplitudes before and after application of 200 nM ω-agatoxin TK (bottom, n = 6, error bars represent SEM). E. Application of the mu-opioid receptor agonist, DAMGO, results in the complete abolition of light-evoked SuM inhibitory transmission. E1, sample traces (top, control in red, DAMGO in grey) and summary graph of light-evoked IPSC amplitudes recorded in CA2 PNs before and after application of 1 μM DAMGO (bottom, n = 6, error bars represent SEM). E2, sample traces (top, SR95531 & CGP55845A in black, DAMGO in grey) and summary graph of light-evoked EPSC amplitudes before and after application of 1μM DAMGO (bottom, n = 17, error bars represent SEM). F. Application of the delta-opioid receptor agonist, DPDPE, results in the long-term depression of light-evoked SuM inhibitory transmission. F1, sample traces (top, control in red, DPDPE in grey) and summary graph of light-evoked IPSC amplitudes before and after application of 0.5 μM DPDPE (bottom, n = 7, error bars represent SEM). F2, sample traces (top, SR95531 & CGP55845A in black,

DAMGO in grey) and summary graph of light-evoked EPSC amplitudes before and after application of 0.5 μM DPDPE (bottom, n = 7, error bars represent SEM).

Figure 6. Area CA2 PNs receive a net inhibitory drive from SuM that controls AP firing properties. A. Diagram illustrating whole-cell recordings of area CA2 PNs and SuM fiber light stimulation in acute slice preparation. B. Example traces of a CA2 PN action potential firing in response to current injection in the absence (black traces) or presence of 10 Hz photostimulation of SuM inputs (red traces). C. Action potential onset latency is increased with 10 Hz SuM input photostimulation. Left, sample traces of the first AP in control and with inhibition blocked by 1 μM SR95531 & 2 μM CGP55845A application (light-off in black, light-on in red, light-off in SR95531 & CGP55845A in grey, light-on in SR95531 & CGP55845A in purple). Right, summary graph of photostimulation-induced delay of AP firing in area CA2 PNs before and after application of SR95531 & CGP55845A (control shown in red, n = 12, paired-T test, p = 0.016; SR95531 & CGP55845A shown in purple, n = 6; Wilcoxon signed-rank test, p = 0.44; individual cells shown with dots, boxplot represents median, quartiles, 10th and 90th percentiles). D. Sample traces of AP firing in repeated trials (light-off in black, light-on in red, light-on in SR95531 & CGP55845A in purple; during experiment photostimulation was interleaved with control but traces are grouped here for demonstration purposes). E. AP jitter in CA2 PNs is reduced by activation of SuM inputs. Left, summary graph of the standard deviation of AP firing with or without 10 Hz photostimulation (n = 12; Wilcoxon signed-rank test, p < 0.001 for the first AP, p = 0.008 for the second AP, p = 0.004 for the third AP; individual cells shown with thin lines, population average shown as thick line, error bars represent SEM). Right, photostimulation-induced reduction of AP firing standard deviation in control and in SR95531 & CGP55845A (control, n = 12; Wilcoxon signed-rank tests, p < 0.001 for the first AP, p = 0.008 for the second AP, p = 0.004 for the third AP; SR95531 & CGP55845A, n = 6; Wilcoxon signed-rank tests, p = 0.22 for the first AP, p = 0.16 for the second AP, p = 0.09 for the third AP; individual cells shown with dots, boxplot represents median, quartiles, 10th and 90th percentiles).

Figure 7. SuM input shapes CA2 PN AP bursts in conditions of elevated cholinergic tone. A. Diagram illustrating whole-cell recordings of area CA2 PNs with light stimulation of SuM fibers in an acute slice preparation. B. Sample trace of spontaneous AP bursting activity recorded from a CA2 PN during bath application of 10 μM CCh. For every even-numbered

burst, a 10 Hz photostimulation (blue bars) was delivered to excite SuM inputs in area CA2 allowing a comparison of burst AP firing in the same cell. C. Sample traces of AP firing during bursts for light-off (left, black) and light-on (right, red) epochs. D. Comparison of AP number per burst for light-off (black) and light-on (red) events (n = 7; individual cells shown as thin lines, population average shown as thick line, error bars represent SEM; paired-T test, $p = 0.031$). E. Average firing rate during spontaneous burst events with SuM photostimulation (red, light-on) and controlled interleaved burst events (black, light-off). Shaded area represents SEM for 7 cells each with between 3 and 13 bursts analyzed in light-on and light-off conditions (2-way ANOVA, light factor: $p < 0.001$, time factor: $p < 0.001$, light x time factor: $p = 0.052$). F. Example burst events with (red) and without (black) SuM photostimulation overlayed and on a scale that shows the rapidly hyperpolarizing membrane potential that occurs with SuM input stimulation. G. Comparison of bursts duration for events with (red) and without (black) photostimulation (n = 7; individual cells shown as thin lines, population average shown as thick line, error bars represent SEM; paired-T test, $p = 0.037$). H. Comparison of time elapsed to next burst onset following bursts with (red) or without (black) photostimulation (n = 7; individual cells shown as thin lines, population average shown as thick line, error bars represent SEM; paired-T test, $p = 0.001$)**.**

Figure 8. Consequences of SuM input on area CA2 output to CA1. A. Diagram illustrating *in vivo* recording in CA1 with tetrodes and SuM axon terminals stimulation over CA2 with an implanted optical fiber. B. Representative data from 4 multi-unit recordings. Raster plot (top) showing CA1 AP firing activity before and during photostimulation of SuM fibers in area CA2. The corresponding firing rate histogram (middle) of four tetrodes placed in the CA1 pyramidal cell layers, as well as plots of standard deviation (SD; bottom). Red lines indicate +/- 3SD. C. Individual (grey) and average (red) normalized firing rates from 34 multiunit recordings, 3 consecutive light stimulation epochs are displayed to help visualizing the consistency of the effect of SuM input light stimulation over area CA2 on CA1 multi-unit firing; the shaded area represents the SEM. D. Diagram illustrating whole-cell recordings of area CA1 PNs and SuM fiber light stimulation over area CA2 in acute slice preparation. E-H. Example waterfall plots (E, G) and corresponding peri-stimulus time histogram (F, H, population average shown as thick line, shaded area represents SEM) of EPSCs (black) and IPSCs (red) recorded from a CA1 PN *ex vivo* during photostimulation of SuM input over area CA2 with bath application of 10 μM CCh.

Supplemental figure legends

Supplemental Figure 1.

A. Diagram illustrating the intersectional strategy used to label CA2-projecting SuM neurons. B-E. Labelling of CA2-projecting SuM neurons with the retrograde CAV-2 carrying Cre-recombinase injected in CA2 and the anterograde AAV carrying DIO-EGFP injected in SuM of wild type mice. B. Labelling of SuM fibers in the hippocampus from CA2-projecting SuM neurons. Left, nissl staining (blue) and EGFP expression (green) in the hippocampus. Right, PCP4 staining (magenta) and EGFP expression (green) in area CA2. C. Retrograde-labeled SuM neurons that project to hippocampal area CA2. Left, nissl staining (blue) and EGFP expression (green) in SuM (mtg = mammillotegmental tract, rmx = retromammillary decussation, SuMl = lateral SuM, SuMm = medial SuM, pm = principal mammillary tract, MM = medial mammillary nucleus). Right, calretinin staining (magenta) and EGFP expression (green) in SuM. D. Higher magnification image of CA2-projecting SuM neurons. Left, nissl staining (blue) and EGFP expression (green) in SuM. Center, nissl (blue) and calretinin staining (magenta) in SuM. Right, calretinin staining (magenta) and EGFP expression (green) in SuM. E. VGluT2 expression of CA2-projecting SuM neurons. Left, nissl staining (blue) and EGFP expression (green) in SuM. Right, VGluT2 staining (red) and EGFP expression (green) in SuM. F. Top, diagram illustrating the injection of AAVs into the SuM. Bottom, sagittal image of the injection site in SuM to express hCHR2(H134R)-EYFP (green) in the VGluT2-Cre line. G-H. Anterograde labelling of SuM projections to the hippocampus from AAV carrying DIO-ChR2-EYFP injected in SuM of VGluT2-Cre mice. G. Left, VGluT2 (red) and nissl staining (blue) in the hippocampus. Right, hCHR2(H134R)-EYFP -expressing SuM fibers (green) and nissl (blue) staining in the hippocampus. H. Left, higher magnification image of area CA2 with VGluT2 (red) and nissl (blue) staining. Center, hCHR2(H134R)-EYFP -expressing SuM fibers (green) and nissl staining (blue). Right, hCHR2(H134R)-EYFP -expressing SuM fibers (green) and VGluT2 staining (red).

Supplemental Figure 2.

A. Diagram illustrating the whole-cell recording configuration of PNs in area CA2 and SuM fiber stimulation in acute hippocampal slices. B. Light-evoked EPCSs from SuM inputs are completely blocked following application of tetrodotoxin (TTX). Sample traces (top, control shown in black, +TTX shown in grey) and power-response curves (bottom) of light-evoked EPSC amplitudes recorded in PN before (black) and after application of 0.2 μM TTX (grey) at different light intensities (n = 5, error bars represent SEM). C. Light-evoked EPCSs from SuM

inputs are completely blocked following application of NMDA and AMPA receptor blockers (NBQX & APV). Sample traces (top, control shown in black, NBQX & APV shown in grey) and time course (bottom) of light-evoked EPSC amplitudes upon application of 10 μM NBQX & 50 μM APV (n = 6, error bars represent SEM).

Supplemental Figure 3.

A. Diagram illustrating the whole-cell recording configuration of hM4D(Gi)-mCherry DREADD-expressing PV INs in area CA2 and SuM fiber stimulation in acute hippocampal slices. B. Time course of the change of membrane potential (V_M) level of Gi-DREADD-expressing CA2 PV INs with application of 10 μM CNO (n = 6, error bars represent SEM). C. V_M level before and after application of CNO (n = 6; Wilcoxon signed-rank test, p = 0.031; individual cells shown as thin lines, population averages shown as thick lines, error bars represent SEM). D. Sample traces of PSPs and spikes recorded from a Gi-DREADD-expressing CA2 PV IN before (left, PSPs in black, spikes in red) and after CNO application (right, PSPs in grey, spikes in light red). E. Same as D with traces displayed as waterfall.

Supplemental Figure 4.

A. Diagram illustrating the whole-cell recording configuration of PNs in area CA2 and SuM fiber stimulation in acute hippocampal slices. B-C. Effect of 10 μM CCh on SuM light-evoked PSCs recorded in CA2 PNs under different conditions: voltage clamp at -70 mV with inhibitory transmission blocked (B, SR95531 & CGP55845A in grey, SR95531 & CGP55845A + CCh in orange), and voltage clamp at +10 mV (C, control in red, CCh in orange). Left, sample traces. Middle, power-response curves (B, n = 7; two-way ANOVA with repeated measures, $p < 0.001$; C, n = 17; two-way ANOVA with repeated measures, $p < 0.001$; error bars represent SEM). Right, comparison of PPRs (B, n = 7; paired-T test, $p < 0.001$; C, n = 17; paired-T test, p = 0.001; individual cells shown as grey lines, population average shown as horizontal line, error bars represent SEM). D-G. Short term dynamics of PSCs evoked by repeated SuM input stimulation at 10 Hz within the same CA2 PNs in voltage clamp at -70 mV or +10 mV. Both SuM-evoked EPSCs and IPSCs were recorded in the same cells before and after application of 10 μM CCh (EPSCs before CCh in black, EPSCs after CCh in grey, IPSCs before CCh in red, IPSCs after CCh in orange; n = 13; error bars represent SEM). D. Sample traces. E. PSC amplitude. F. Pulse #n over pulse #1 ratio. G. E/I ratio. See Supplemental Table 1 for statistics.

Table 1. Electrophysiological properties of pyramidal neurons in SuM-innervated area

	V_M (mV)	R_M (MOhm)	C_M (pF)
CA2 PN (n = 81)	-69.8 ± 0.70	59.2 ± 2.65	209 ± 11.4
CA3 PN (n = 31)	-70.3 ± 1.06	72.4 ± 4.82	211 ± 15.7
Statistics	Mann-Whitney U test p = 0.997	Student T test p = 0.020*	Mann-Whitney U test p = 0.625
PN deep (n = 57)	-71.1 ± 0.76	64.0 ± 3.94	200 ± 12.3
PN superficial (n = 76)	-69.3 ± 0.67	64.9 ± 3.19	196 ± 11.8
Statistics	Student T test p = 0.077	Mann-Whitney U test p = 0.777	Mann-Whitney U test p = 0.588

Table 2. Characteristics of SuM light-evoked transmission onto pyramidal neurons

	EPSC					
cell type	connectivity (%)	amplitude (pA)	rise time (ms)	decay time (ms)	latency (ms)	success rate
CA2 PN	56 (n = 58 of 103)	-16 ± 1.9	2.9 ± 0.1	14 ± 0.8	2.4 ± 0.2	0.44 ± 0.03
CA3 PN	49 (n = 22 of 45)	-23 ± 5.9	3.0 ± 0.2	14 ± 0.9	2.7 ± 0.3	0.56 ± 0.06
Statistics	χ^2 test p = 0.572	Mann-Whitney U test p = 0.409	Mann-Whitney U test p = 0.391	Mann-Whitney U test p = 0.797	Mann-Whitney U test p = 0.156	Student T test p = 0.074
PN deep	56 (n = 35 of 63)	-15 ± 2.0	3.5 ± 0.2	16 ± 1.0	3.5 ± 0.4	0.39 ± 0.03
PN superficial	56 (n = 53 of 94)	-20 ± 3.0	3.1 ± 0.2	15 ± 0.9	2.7 ± 0.3	0.51 ± 0.04
Statistics	χ^2 test p = 0.946	Mann-Whitney U test p = 0.306	Mann-Whitney U test p = 0.051	Mann-Whitney U test p = 0.314	Mann-Whitney U test p = 0.083	Mann-Whitney U test p = 0.072
	IPSC					
cell type	connectivity (%)	amplitude (pA)	rise time (ms)	decay time (ms)	latency (ms)	success rate
CA2 PN	35 (n = 19 of 55)	197 ± 41.3	3.8 ± 0.4	25 ± 1.2	6.3 ± 0.7	0.55 ± 0.06
CA3 PN	57 (n = 16 of 28)	145 ± 23.4	4.5 ± 0.4	25 ± 1.2	7.5 ± 0.9	0.54 ± 0.05
Statistics	χ^2 test p = 0.134	Mann-Whitney U test p = 0.870	Student T test p = 0.203	Mann-Whitney U test p = 0.896	Mann-Whitney U test p = 0.303	Student T test p = 0.893
PN deep	47 (n = 16 of 34)	199 ± 40.6	3.8 ± 0.4	25 ± 1.4	7.2 ± 0.8	0.52 ± 0.07
PN superficial	47 (n = 26 of 55)	167 ± 27.5	4.9 ± 0.4	26 ± 1.2	6.8 ± 0.7	0.50 ± 0.05
Statistics	χ^2 test p = 0.987	Mann-Whitney U test p = 0.258	Student T test p = 0.047*	Student T test p = 0.564	Student T test p = 0.706	Student T test p = 0.796

Table 3. Electrophysiological properties of interneurons in SuM-innervated area

	V_M (mV)	R_M (MOhm)	C_M (pF)	firing adaptation index	sag (mV)
Basket cell (n = 16)	-57.3 ± 1.38	144 ± 28.1	64.0 ± 8.70	0.74 ± 0.05	9.4 ± 1.0
non-Basket Cell (n = 12)	-55.6 ± 1.84	224 ± 46.8	52.0 ± 5.90	0.57 ± 0.06	5.9 ± 1.4
interneuron SO (n = 6)	-57.0 ± 3.16	201 ± 21.0	44.7 ± 5.31	0.61 ± 0.11	7.6 ± 1.9
interneuron SR (n = 8)	-60.1 ± 2.89	282 ± 49.8	39.6 ± 3.18	0.65 ± 0.09	8.1 ± 2.1
Statistics	1-way ANOVA test p = 0.527	1-way ANOVA test p = 0.100	Kruskal-Wallis test p = 0.354	1-way ANOVA test p = 0.238	1-way ANOVA test p = 0.292

Table 4. Characteristics of excitatory SuM light-evoked transmission onto interneurons & pyramidal cells

cell type	connectivity (%)	amplitude (pA)	rise time (ms)	decay time (ms)	latency (ms)	success rate
Pyramidal Cell	63 (n = 166 of 263)	-19 ± 1.6*	3.4 ± 0.1*	15 ± 0.5*	2.9 ± 0.1	0.46 ± 0.02
Basket Cell	82 (n = 18 of 22)	-43 ± 8.7*	1.7 ± 0.3*	8.4 ± 1.3*	3.1 ± 0.4	0.59 ± 0.07
non-Basket Cell interneuron SO interneuron SR	39 (n = 10 of 26) 12 (n = 2 of 17) 11 (n = 1 of 9)	-16 ± 2.8	2.6 ± 0.5	12 ± 1.4	3.4 ± 0.7	0.36 ± 0.06
Statistics	χ^2 test p = 0.006*	Kruskal-Wallis test p = 0.016 Dunn-Holland-Wolfe *post hoc* p < 0.05*	1-way ANOVA test p < 0.001 Tukey *post hoc* p < 0.001*	1-way ANOVA test p < 0.001 Tukey *post hoc* p < 0.001*	1-way ANOVA test p = 0.580	1-way ANOVA test p = 0.066

Supplemental Table 1. Statistical comparisons related to Supplemental Figure 4.

Measurement	Conditions	Factors	2-way ANOVA p-values
amplitude	EPSC amplitude +/- CCh (n = 13)	treatment	0.00171693
		pulse #	0.00286193
		treatment x pulse #	0.0521822
	IPSC amplitude +/- CCh (n = 13)	treatment	0.413564
		pulse #	0.0247487
		treatment x pulse #	0.316489
	PSC amplitude in ACSF (n = 13)	holding level	0.0121691
		pulse #	0.0115431
		holding level x pulse #	0.391097
	PSC amplitude in CCh (n = 13)	holding level	2.85112E-11
		pulse #	0.189593
		holding level x pulse #	0.55014
Pn/P1 ratio	EPSC Pn/P1 ratio +/- CCh (n = 13)	treatment	1.05342E-10
		pulse #	9.99201E-16
		treatment x pulse #	0.0110396
	IPSC Pn/P1 ratio +/- CCh (n = 13)	treatment	0.000184435
		pulse #	0.00209369
		treatment x pulse #	0.297716
	PSC Pn/P1 ratio in ACSF (n = 13)	holding level	0.325751
		pulse #	2.08101E-08
		holding level x pulse #	0.941122
	PSC Pn/P1 ratio in CCh (n = 13)	holding level	0.0948351
		pulse #	3.07005E-05
		holding level x pulse #	0.889375
E/I ratio	PSC E/I ratio +/- CCh (n = 13)	treatment	7.61696E-06
		pulse #	0.99245
		treatment x pulse #	0.982047

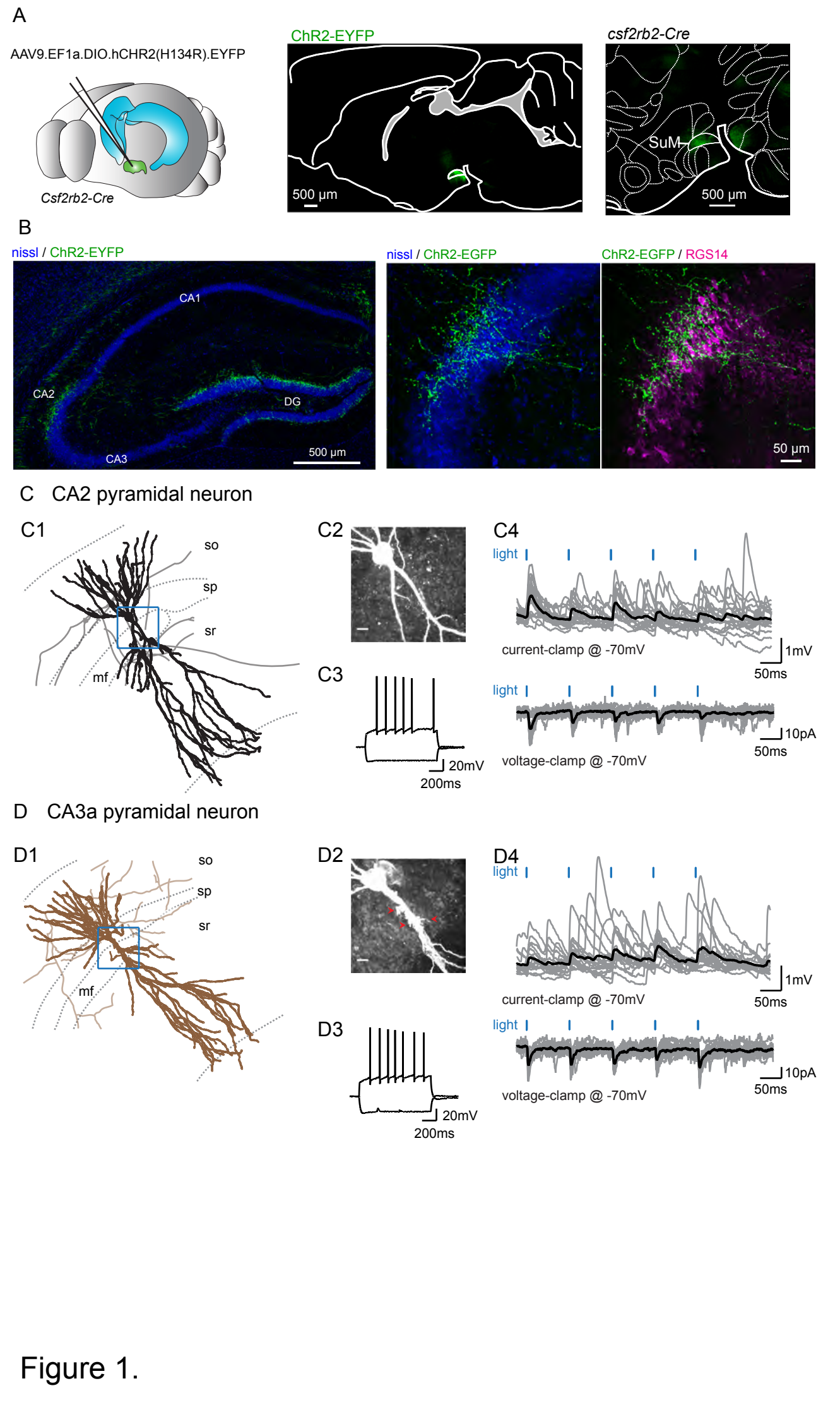
A
AAV9.EF1a.DIO.hCHR2(H134R).EYFP
Csf2rb2-Cre
ChR2-EYFP
500 μm
csf2rb2-Cre
SuM
500 μm
B
nissl / ChR2-EYFP
CA1
CA2
DG
CA3
500 μm
nissl / ChR2-EGFP
ChR2-EGFP / RGS14
50 μm
C CA2 pyramidal neuron
C1
so
sp
sr
mf
C2
C3
20mV
200ms
C4
light
current-clamp @ -70mV
1mV
50ms
light
10pA
50ms
voltage-clamp @ -70mV
D CA3a pyramidal neuron
D1
so
sp
sr
mf
D2
D3
20mV
200ms
D4
light
current-clamp @ -70mV
1mV
50ms
light
10pA
50ms
voltage-clamp @ -70mV

Figure 1.

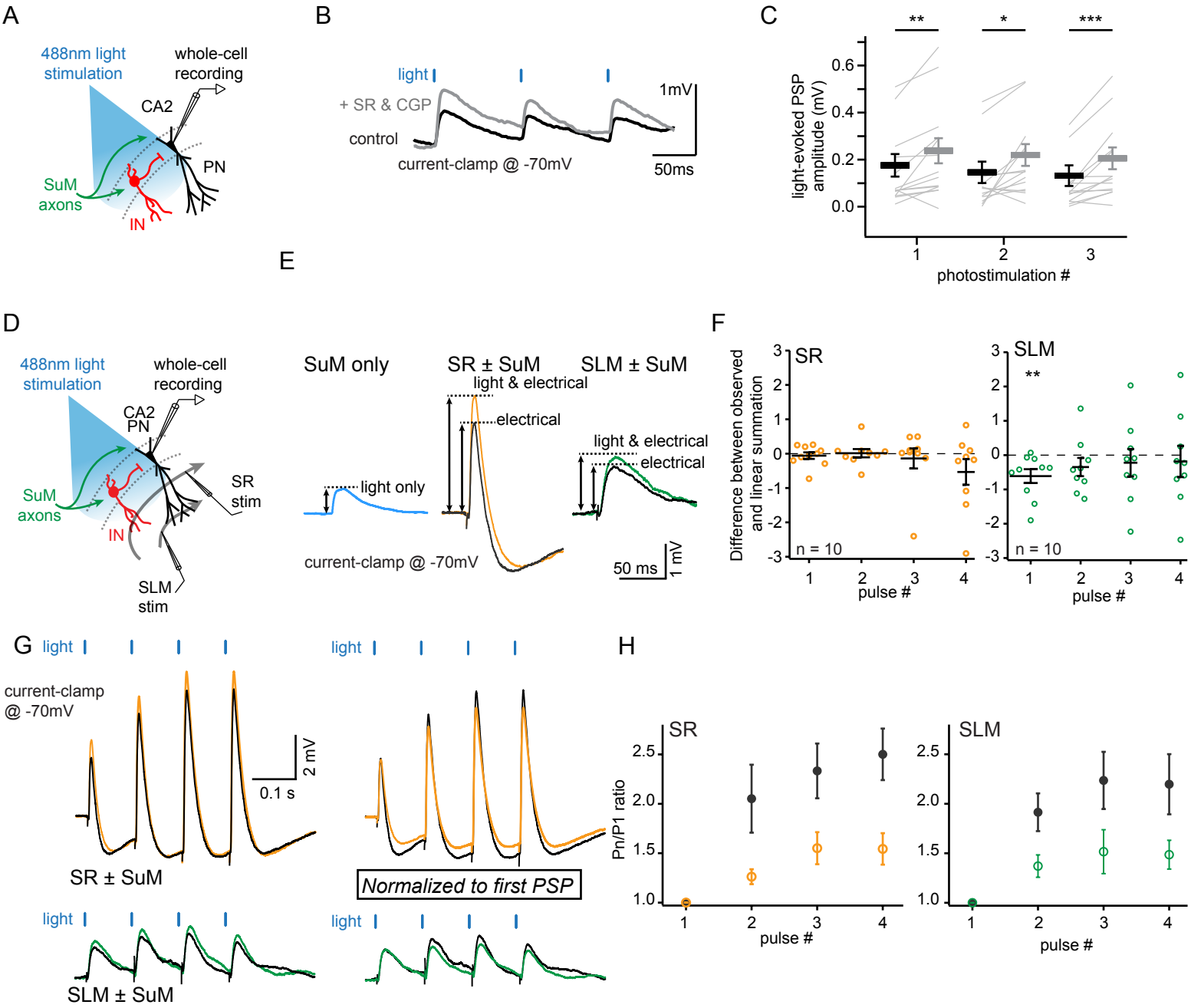
A
488nm light stimulation
whole-cell recording
CA2
PN
SuM axons
IN
B
light
+ SR & CGP
control
1mV
current-clamp @ -70mV
50ms
C
**
*
***
light-evoked PSP amplitude (mV)
0.6
0.4
0.2
0.0
1
2
3
photostimulation #
E
D
488nm light stimulation
whole-cell recording
CA2
PN
SuM axons
IN
SR stim
SLM stim
SuM only
SR ± SuM
SLM ± SuM
light & electrical
electrical
light only
light & electrical
electrical
current-clamp @ -70mV
50 ms
1 mV
F
SR
SLM
**
Difference between observed and linear summation
n = 10
n = 10
pulse #
pulse #
G
light
current-clamp @ -70mV
0.1 s
2 mV
SR ± SuM
light
Normalized to first PSP
light
SLM ± SuM
light
H
SR
SLM
Pn/P1 ratio
2.5
2.0
1.5
1.0
pulse #
pulse #

Figure 2.

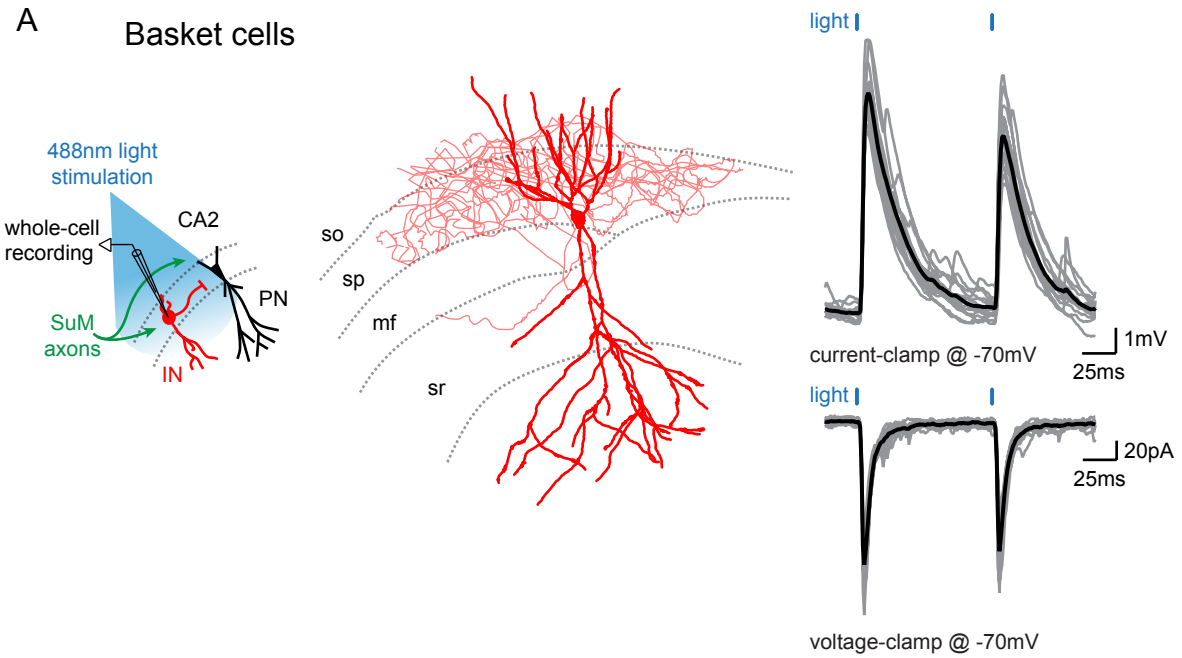
A
Basket cells
488nm light stimulation
whole-cell recording
CA2
PN
SuM axons
IN
so
sp
mf
sr
light
current-clamp @ -70mV
1mV
25ms
light
20pA
25ms
voltage-clamp @ -70mV

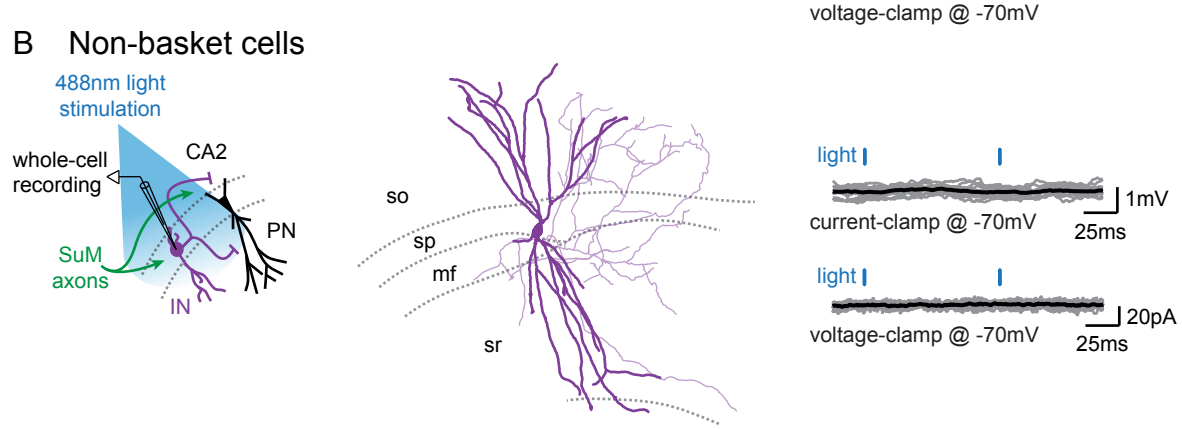
B
Non-basket cells
488nm light stimulation
whole-cell recording
CA2
PN
SuM axons
IN
so
sp
mf
sr
light
current-clamp @ -70mV
1mV
25ms
light
voltage-clamp @ -70mV
20pA
25ms

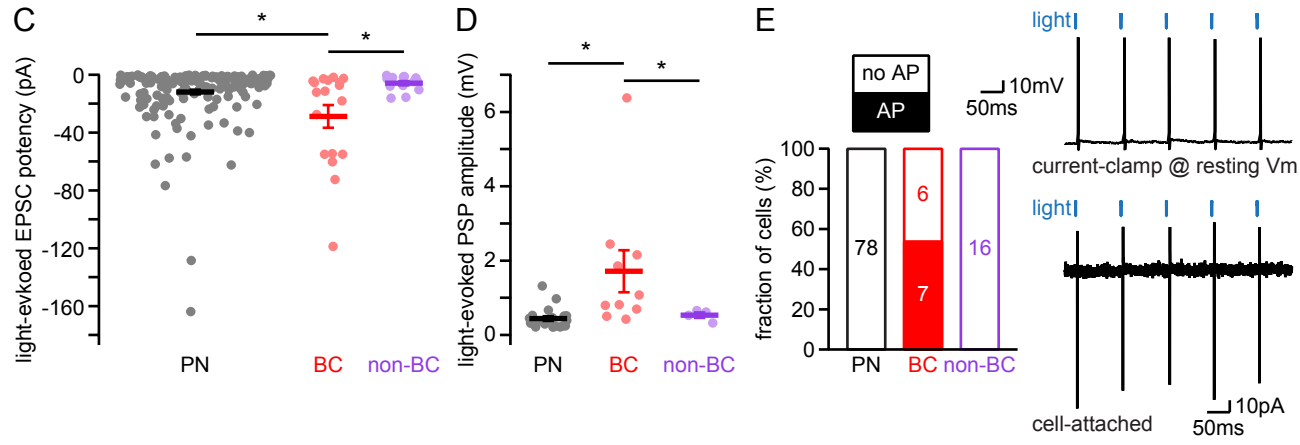
C
light-evkoed EPSC potency (pA)
0
-40
-80
-120
-160
PN
BC
non-BC
*
*
D
light-evoked PSP amplitude (mV)
0
2
4
6
PN
BC
non-BC
*
*
E
no AP
AP
fraction of cells (%)
100
80
60
40
20
0
78
6
7
16
PN
BC
non-BC
light
10mV
50ms
current-clamp @ resting Vm
light
cell-attached
10pA
50ms

Figure 3.

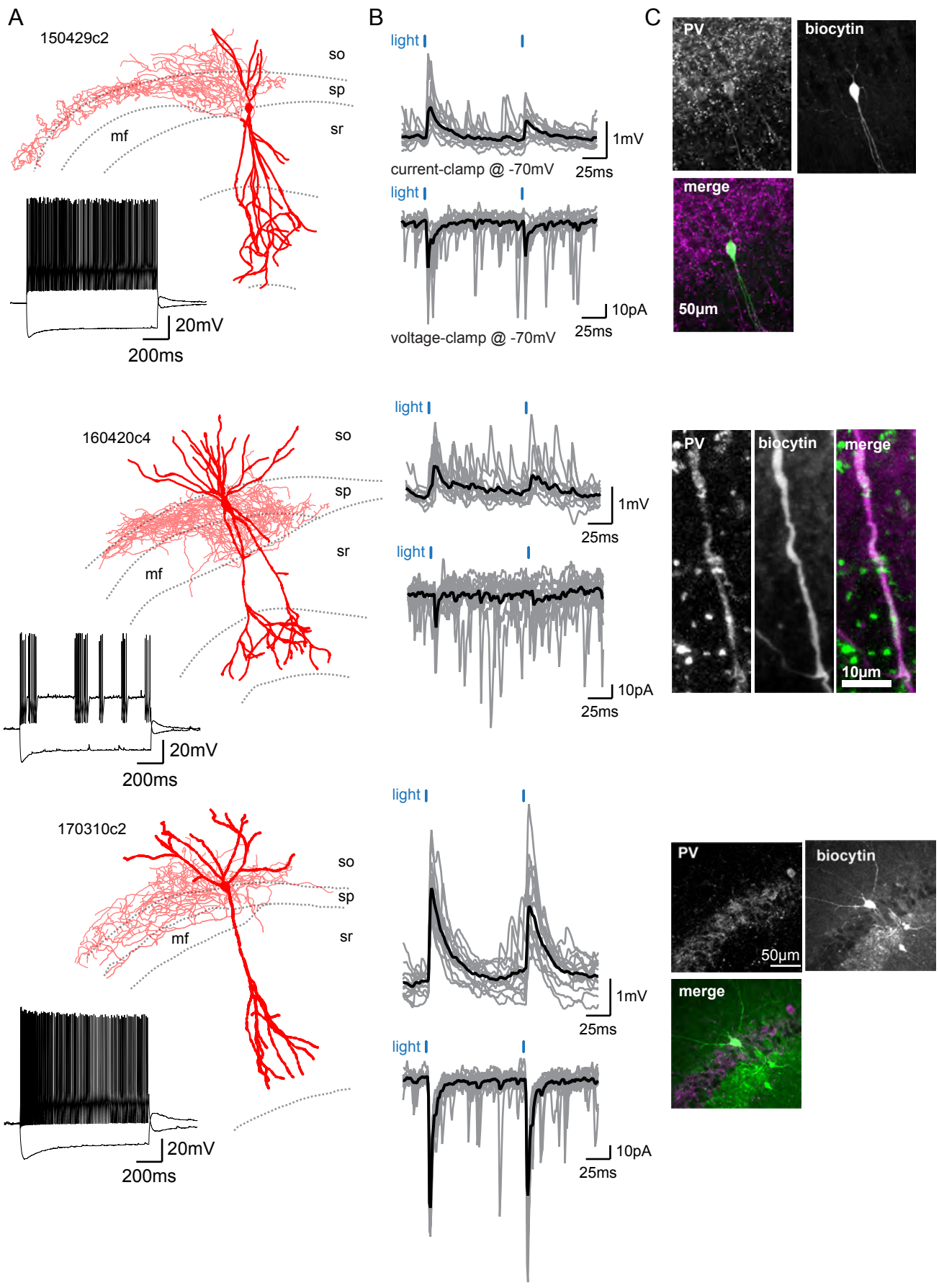
A
150429c2
so
sp
sr
mf
20mV
200ms
B
light
1mV
current-clamp @ -70mV
25ms
light
10pA
voltage-clamp @ -70mV
25ms
C
PV
biocytin
merge
50µm
160420c4
so
sp
sr
mf
20mV
200ms
light
1mV
25ms
light
10pA
25ms
PV
biocytin
merge
10µm
170310c2
so
sp
sr
mf
20mV
200ms
light
1mV
25ms
light
10pA
25ms
PV
50µm
biocytin
merge

Figure 4.

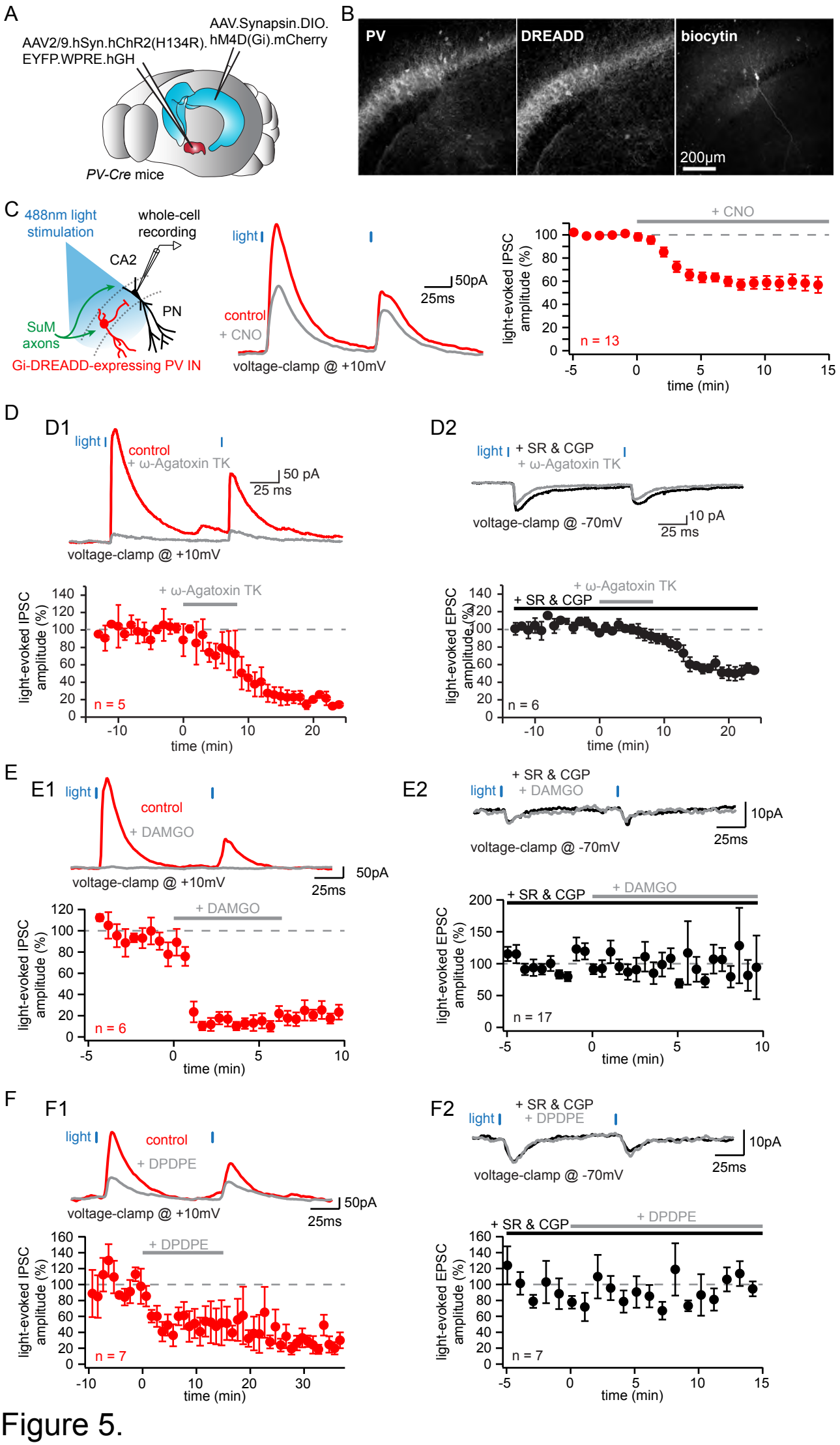
A
AAV2/9.hSyn.hChR2(H134R).
EYFP.WPRE.hGH
AAV.Synapsin.DIO.
hM4D(Gi).mCherry
PV-Cre mice
B
PV
DREADD
biocytin
200µm
C
488nm light
stimulation
whole-cell
recording
CA2
PN
SuM
axons
Gi-DREADD-expressing PV IN
light
control
+ CNO
50pA
25ms
voltage-clamp @ +10mV
+ CNO
light-evoked IPSC
amplitude (%)
n = 13
time (min)
D
D1
light
control
+ ω-Agatoxin TK
50 pA
25 ms
voltage-clamp @ +10mV
+ ω-Agatoxin TK
light-evoked IPSC
amplitude (%)
n = 5
time (min)
D2
light
+ SR & CGP
+ ω-Agatoxin TK
voltage-clamp @ -70mV
10 pA
25 ms
+ ω-Agatoxin TK
+ SR & CGP
light-evoked EPSC
amplitude (%)
n = 6
time (min)
E
E1
light
control
+ DAMGO
voltage-clamp @ +10mV
50pA
25ms
+ DAMGO
light-evoked IPSC
amplitude (%)
n = 6
time (min)
E2
+ SR & CGP
light
+ DAMGO
10pA
25ms
voltage-clamp @ -70mV
+ SR & CGP
+ DAMGO
light-evoked EPSC
amplitude (%)
n = 17
time (min)
F
F1
light
control
+ DPDPE
voltage-clamp @ +10mV
50pA
25ms
+ DPDPE
light-evoked IPSC
amplitude (%)
n = 7
time (min)
F2
+ SR & CGP
light
+ DPDPE
10pA
25ms
voltage-clamp @ -70mV
+ SR & CGP
+ DPDPE
light-evoked EPSC
amplitude (%)
n = 7
time (min)

Figure 5.

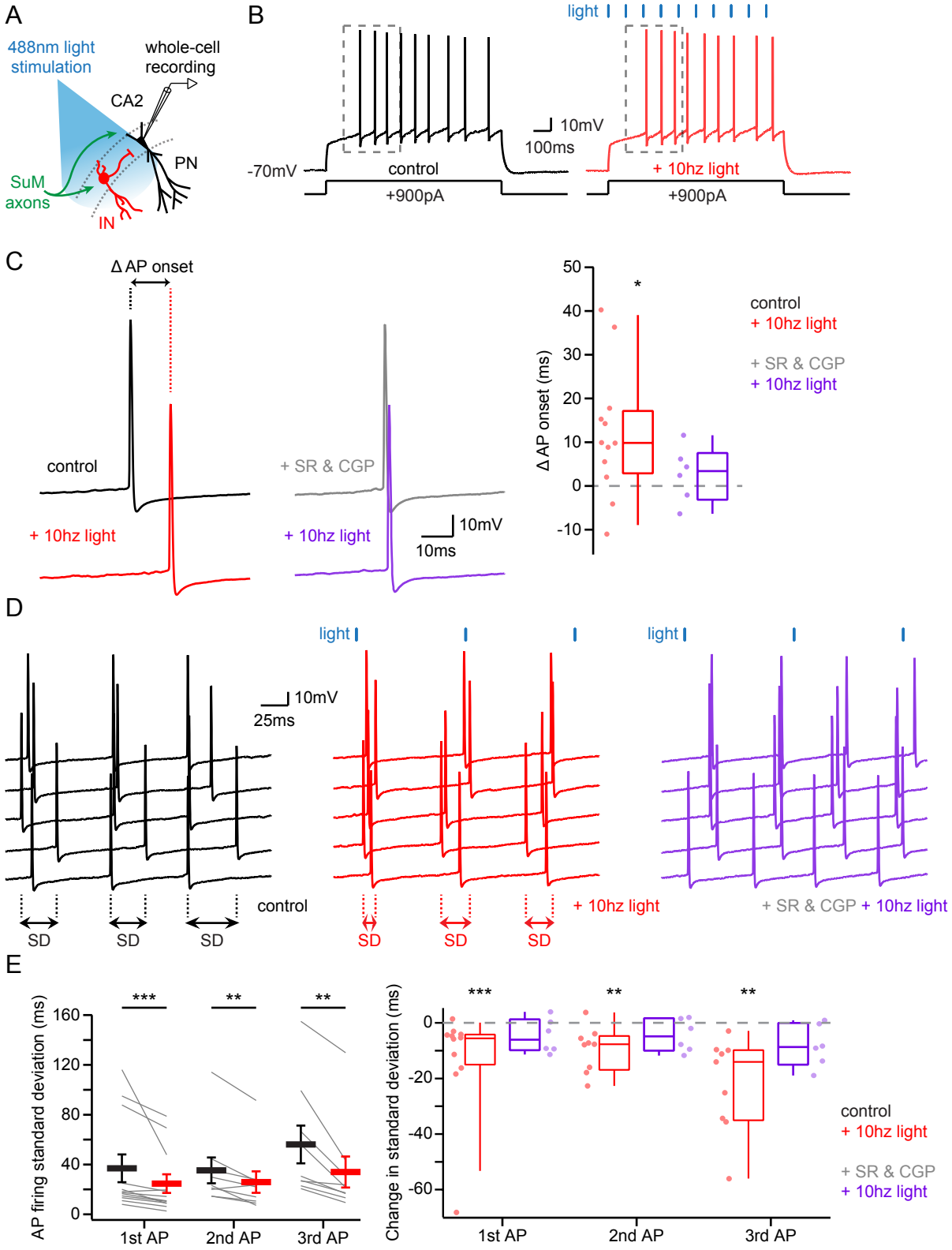
A
488nm light stimulation
whole-cell recording
CA2
PN
SuM axons
IN
B
light
-70mV
control
+900pA
10mV
100ms
+ 10hz light
+900pA
C
Δ AP onset
control
+ 10hz light
+ SR & CGP
+ 10hz light
10mV
10ms
Δ AP onset (ms)
control
+ 10hz light
+ SR & CGP
+ 10hz light
D
light
10mV
25ms
control
SD
+ 10hz light
+ SR & CGP + 10hz light
E
AP firing standard deviation (ms)
1st AP
2nd AP
3rd AP
Change in standard deviation (ms)
control
+ 10hz light
+ SR & CGP
+ 10hz light

Figure 6.

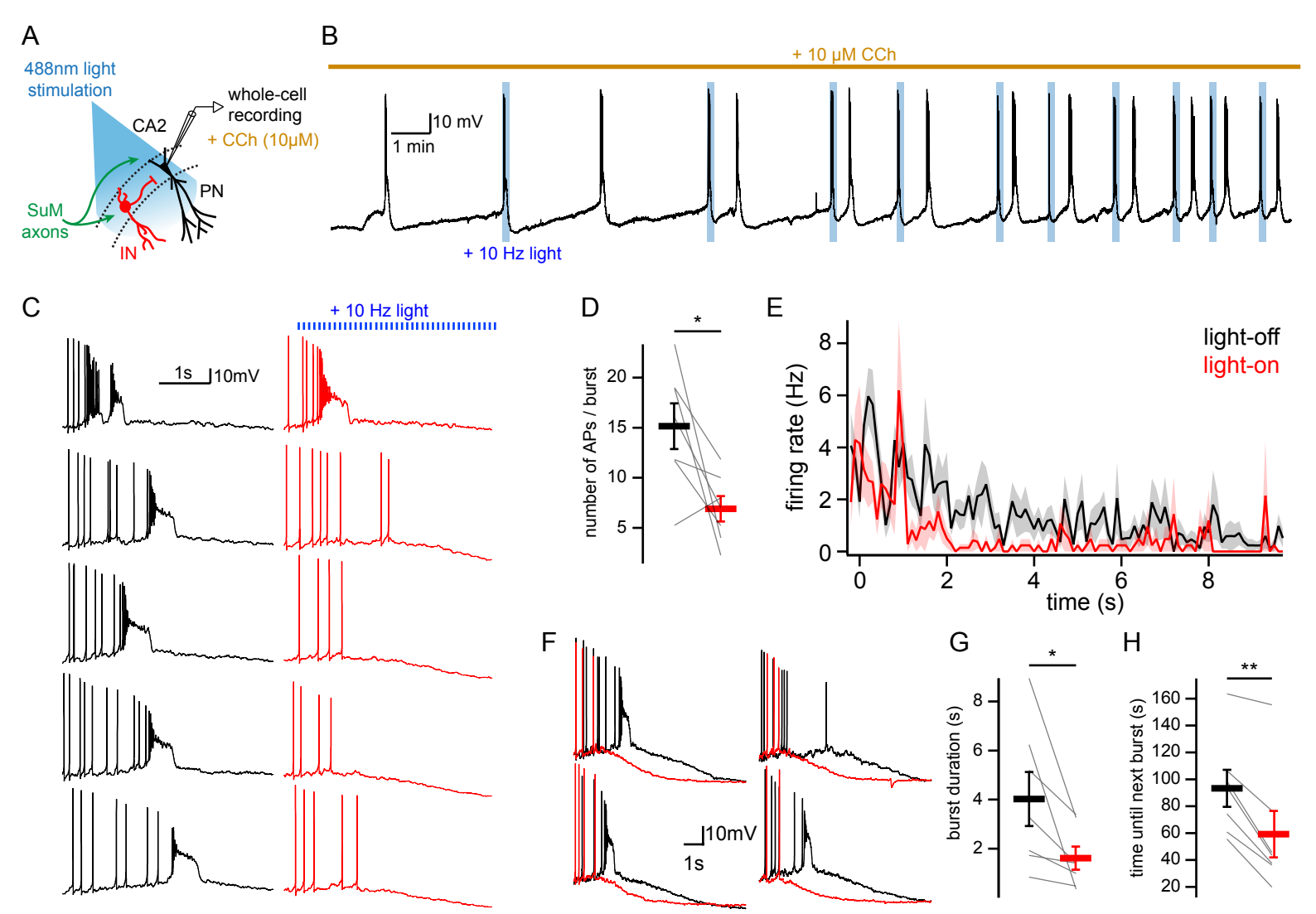
A
488nm light stimulation
CA2
whole-cell recording
+ CCh (10μM)
PN
SuM axons
IN
B
+ 10 μM CCh
10 mV
1 min
+ 10 Hz light
C
+ 10 Hz light
1s
10mV
D
*
number of APs / burst
E
light-off
light-on
firing rate (Hz)
time (s)
F
10mV
1s
G
*
burst duration (s)
H
**
time until next burst (s)

Figure 7.

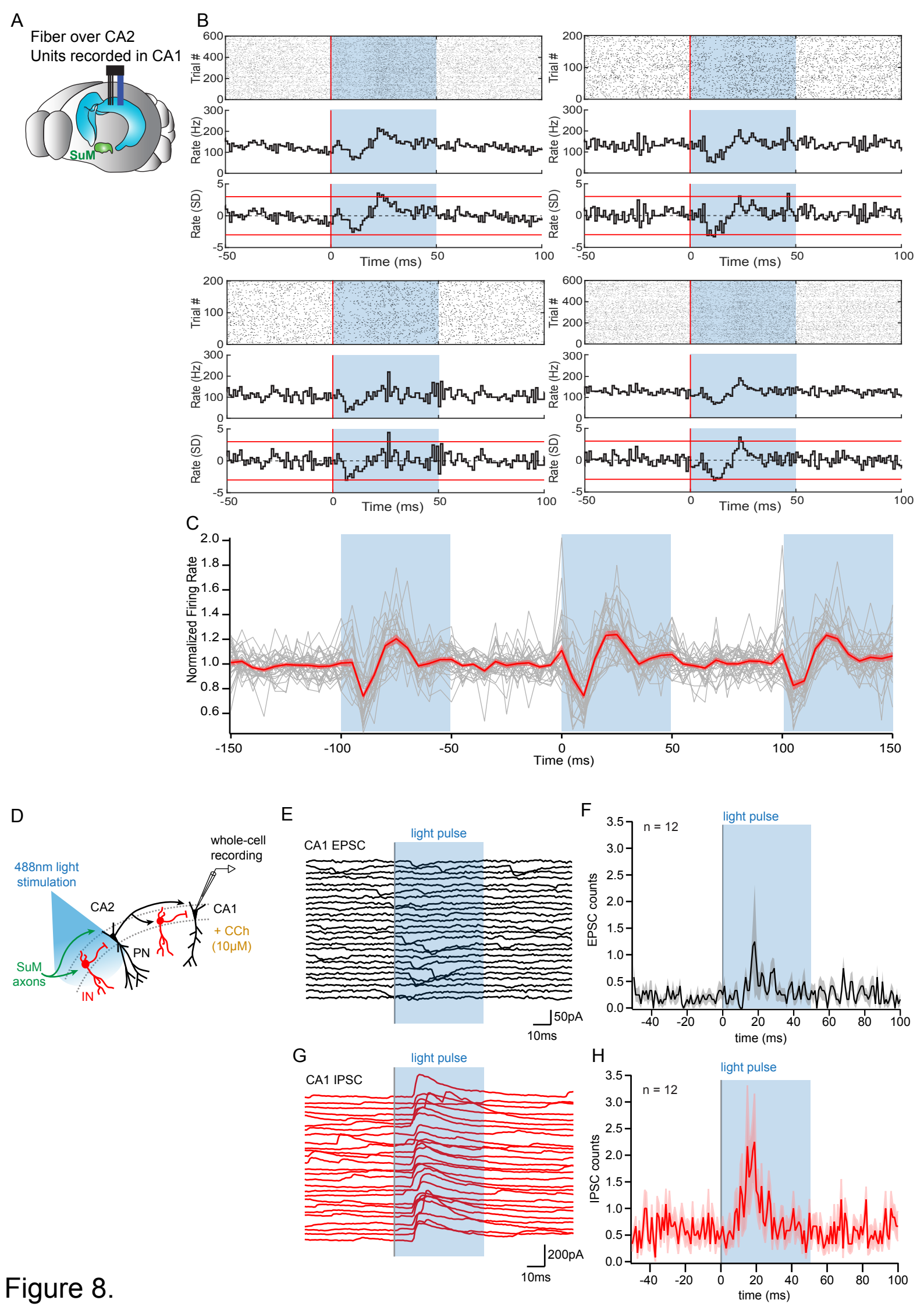
A
Fiber over CA2
Units recorded in CA1
SuM
B
Trial #
Rate (Hz)
Rate (SD)
Time (ms)
C
Normalized Firing Rate
Time (ms)
D
488nm light stimulation
whole-cell recording
CA2
CA1
+ CCh (10μM)
PN
SuM axons
IN
E
CA1 EPSC
light pulse
50pA
10ms
F
n = 12
light pulse
EPSC counts
time (ms)
G
CA1 IPSC
light pulse
200pA
10ms
H
n = 12
light pulse
IPSC counts
time (ms)

Figure 8.

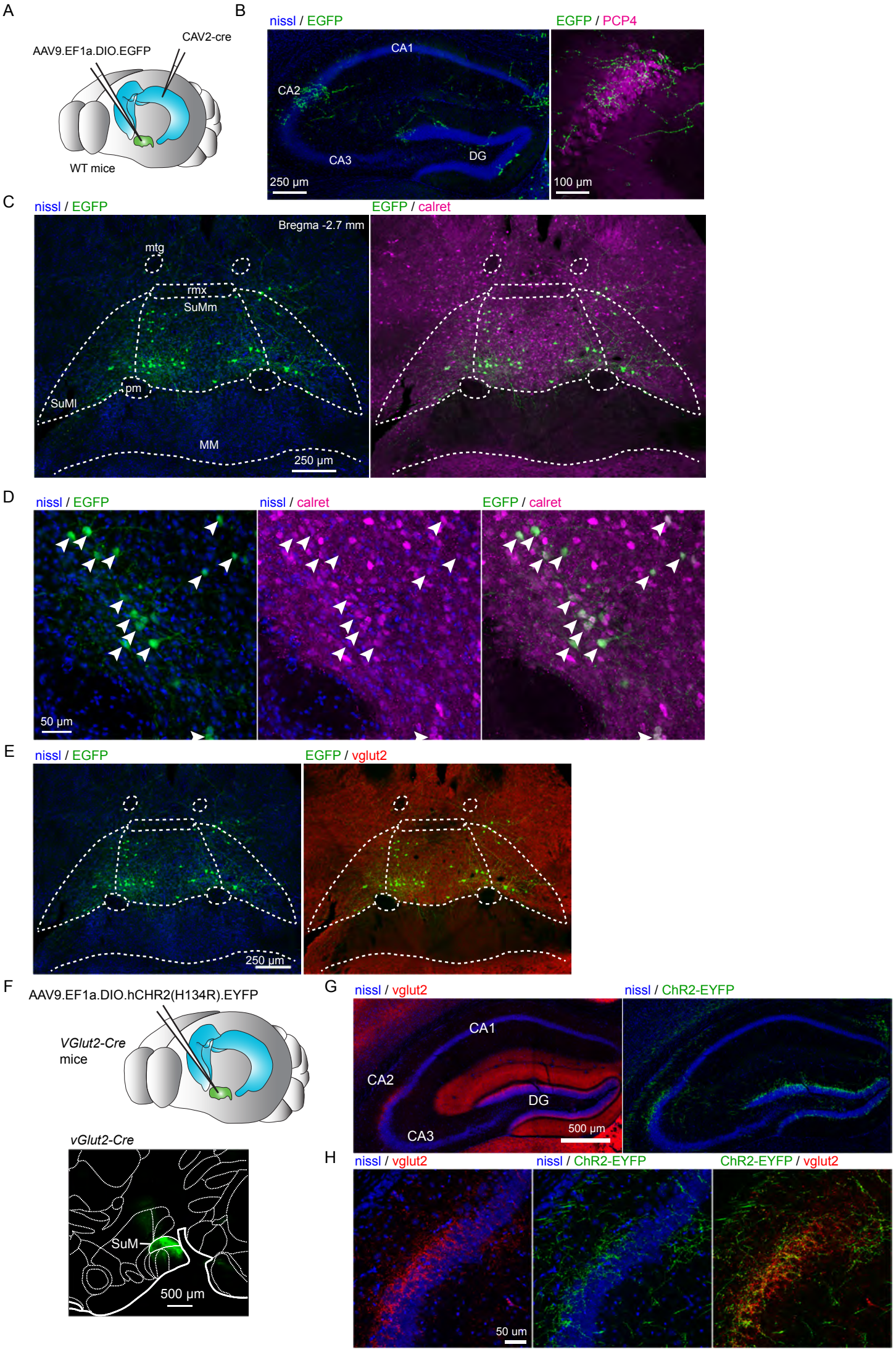

Supplemental Figure 1.

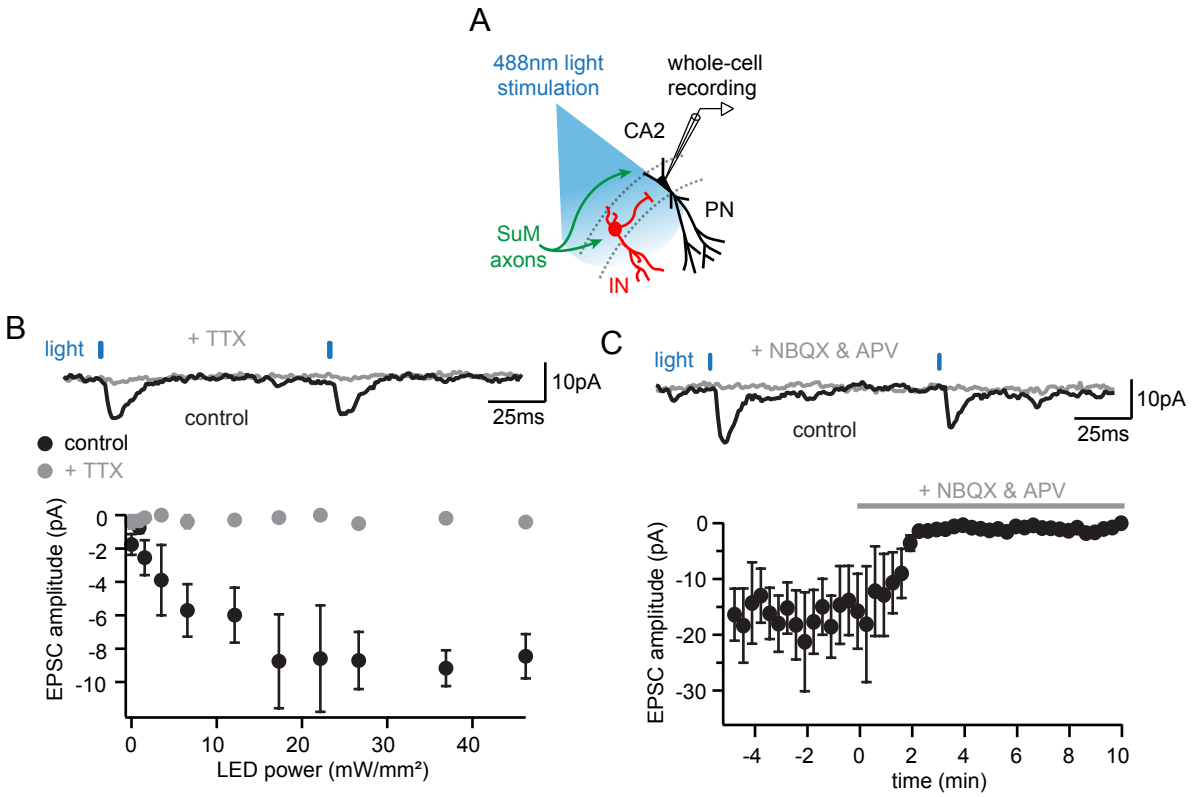

Supplemental Figure 2.

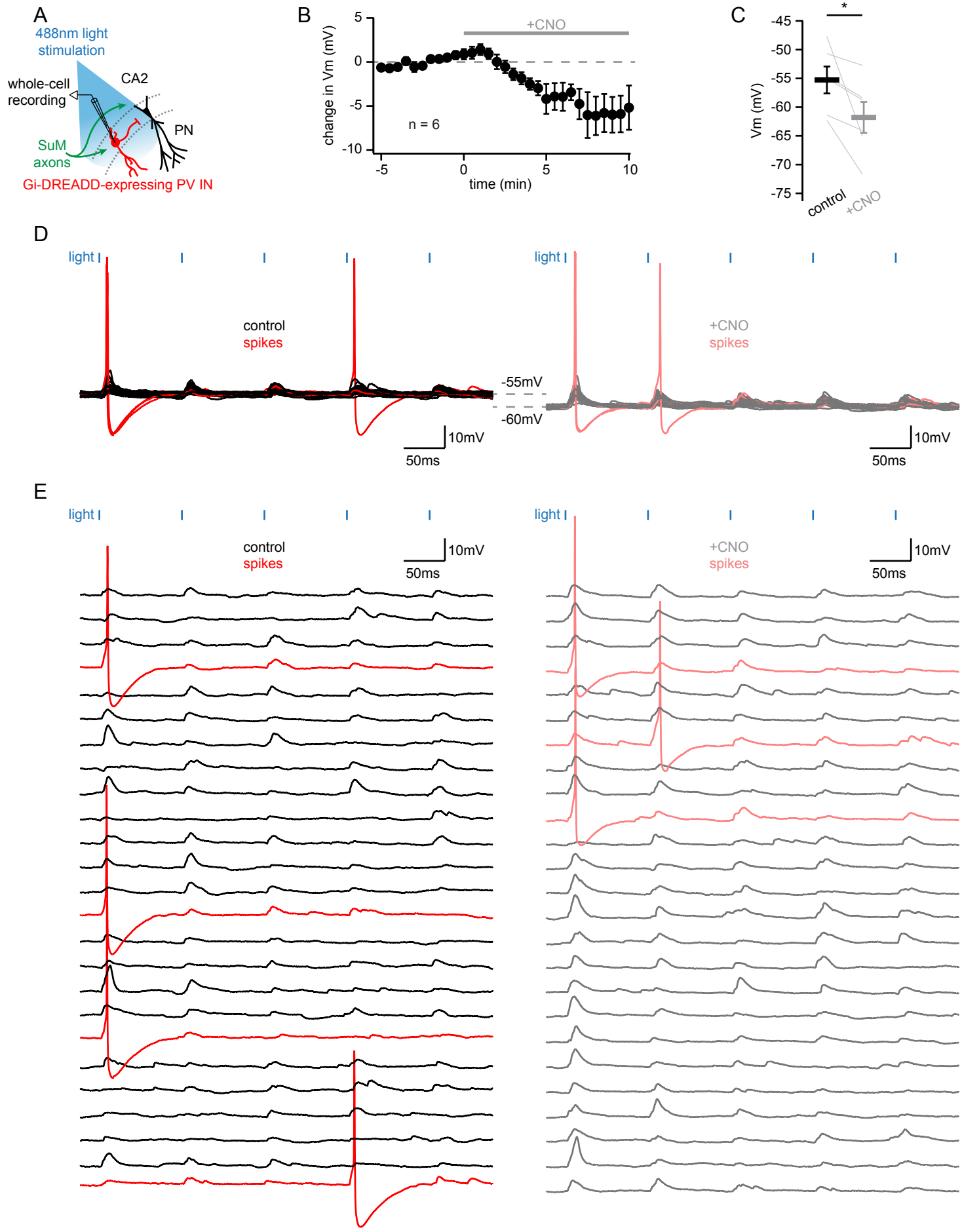

Supplemental Figure 3.

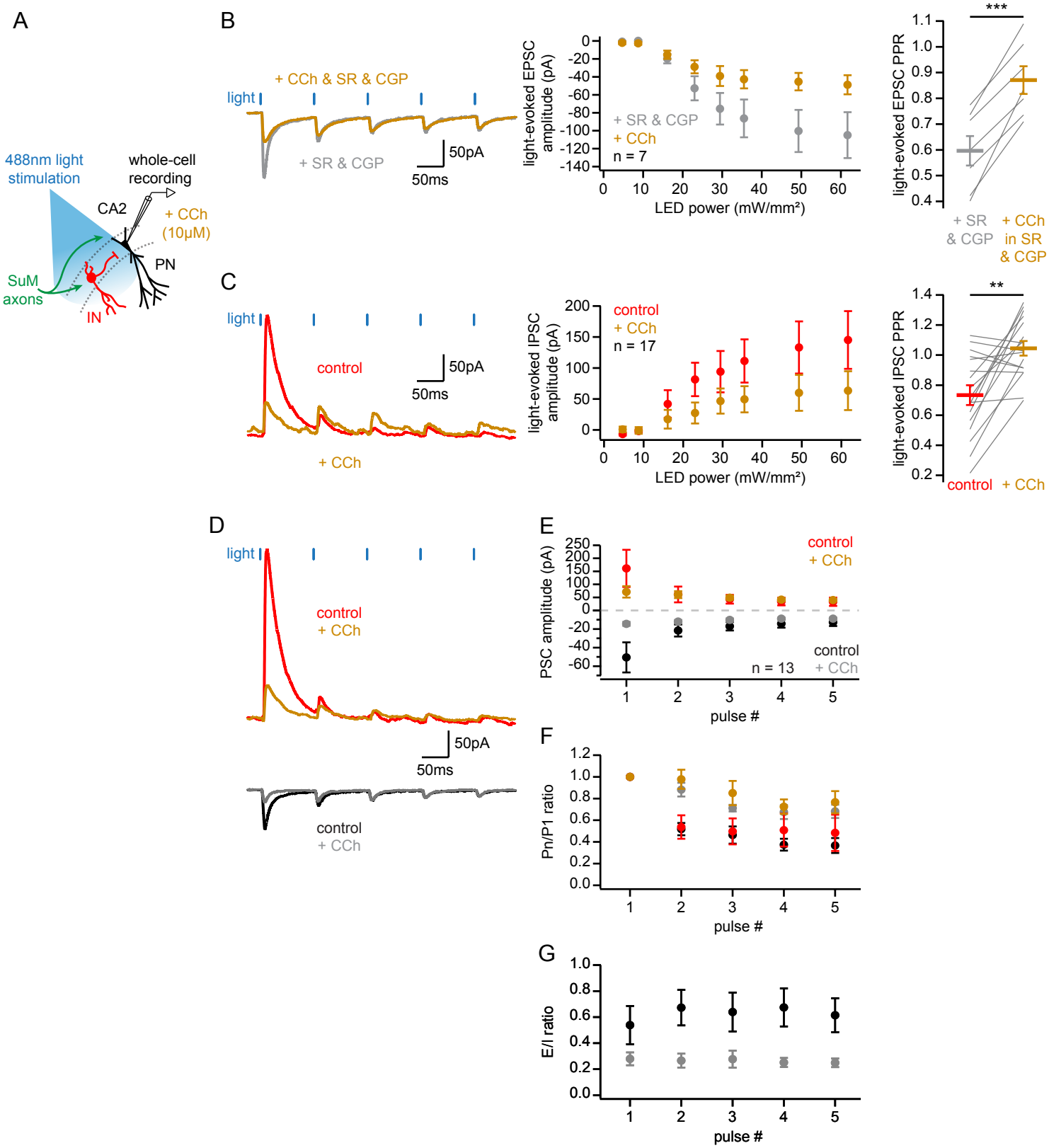

Supplemental Figure 4.